

1 SEARCH FOR $t\bar{t}Z' \rightarrow t\bar{t}t\bar{t}$ PRODUCTION IN THE MULTILEPTON FINAL STATE IN
2 pp COLLISIONS AT $\sqrt{s} = 13$ TEV WITH THE ATLAS DETECTOR

3 By

4 Hieu Le

5 A DISSERTATION

6 Submitted to
7 Michigan State University
8 in partial fulfillment of the requirements
9 for the degree of

10 Physics — Doctor of Philosophy

11 2025

ABSTRACT

13 Lorem ipsum dolor sit amet, consectetur adipiscing elit, sed do eiusmod tempor incididunt ut
14 labore et dolore magna aliqua. Ut enim ad minim veniam, quis nostrud exercitation ullamco
15 laboris nisi ut aliquip ex ea commodo consequat. Duis aute irure dolor in reprehenderit in
16 voluptate velit esse cillum dolore eu fugiat nulla pariatur. Excepteur sint occaecat cupidatat
17 non proident, sunt in culpa qui officia deserunt mollit anim id est laborum.

ACKNOWLEDGMENTS

- 19 Advisor: Reinhard Schwienhorst
- 20 Postdoc: Binbin Dong
- 21 Committee
- 22 MSU group
- 23 ATLAS analysis group
- 24 Friend: Daniel, Grayson, Bella, Eric, Jordan
- 25 Other friends: Jasper, Adam, Brittany
- 26 Parents
- 27 Spouse: Allen Sechrist
- 28 ATLAS in general & funding agencies

PREFACE

30 This is my preface. remarks remarks remarks

TABLE OF CONTENTS

31	List of Tables	vii
32	List of Figures	viii
33	KEY TO ABBREVIATIONS	ix
34	Roadmap	1
35	Chapter 1. Introduction	2
36	Chapter 2. Theoretical Overview	3
37	2.1 The Standard Model	3
38	2.1.1 Elementary particles	3
39	2.1.2 Mathematical formalism	7
40	2.1.2.1 Quantum chromodynamics	8
41	2.1.2.2 Electroweak theory	10
42	2.1.2.3 Higgs mechanism	13
43	2.2 Beyond the Standard Model	16
44	2.2.1 Top-philic vector resonance	16
45	2.2.2 BSM four-top quark production	19
46	Chapter 3. LHC & ATLAS Experiment	21
47	3.1 The Large Hadron Collider	21
48	3.1.1 Overview	21
49	3.1.2 LHC operations	21
50	3.2 The ATLAS detector	22
51	3.2.1 Inner detector	24
52	3.2.2 Calorimeter systems	25
53	3.2.3 Muon spectrometer	27
54	3.2.4 Forward detectors	29
55	3.2.5 Magnetic systems	29
56	3.2.6 Trigger & data acquisition	29
57	Chapter 4. Particle Reconstruction & Identification	31
58	4.1 Primary reconstruction	31
59	4.1.1 Tracks	31
60	4.1.2 Vertices	32
61	4.1.3 Topological clusters	33
62	4.2 Jets	35
63	4.2.1 Flavor tagging	36
64	4.3 Leptons	38
65	4.3.1 Electrons	39

66	4.3.2	Muons	42
67	4.4	Missing transverse momentum	44
68	4.5	Overlap removal	45
69	4.6	Object definition	46
70	Chapter 5. Data & Simulated Samples		47
71	5.1	Data samples	47
72	5.2	Monte Carlo samples	48
73	5.2.1	$t\bar{t}Z'$ signal samples	48
74	5.2.2	Background samples	50
75	Chapter 6. Analysis Strategy		52
76	6.1	Event selection	52
77	6.2	Analysis regions	54
78	6.2.1	Signal regions	54
79	6.2.2	Control regions	55
80	6.2.3	Validation regions	57
81	6.3	Background estimation	57
82	6.3.1	Template fitting for fake/non-prompt estimation	59
83	6.3.2	Charge misidentification data-driven estimation	60
84	6.3.3	$t\bar{t}W$ background data-driven estimation	62
85	Chapter 7. Systematic Uncertainties		66
86	7.1	Experimental uncertainties	66
87	7.1.1	Leptons	66
88	7.1.2	Jets	67
89	7.1.3	Missing transverse energy	69
90	7.2	Modeling uncertainties	69
91	7.2.1	Signal and irreducible background uncertainties	69
92	7.2.2	Reducible background uncertainties	72
93	Chapter 8. Results		75
94	8.1	Statistical analysis	75
95	8.1.1	Profile likelihood fit	75
96	8.1.2	Exclusion limits	77
97	8.2	Fit results	77
98	Chapter 9. Summary		78
99	References		79

List of Tables

101	Table 4.1: Caption	45
102	Table 4.2: Caption	46
103	Table 5.1: Caption	47
104	Table 5.2: Summary of all Monte-Carlo samples used in this analysis.	49
105	Table 6.1: Caption	55
106	Table 6.2: Caption	56
107	Table 6.3: Caption	58
108	Table 7.1: Summary of the experimental systematic uncertainties considered in this	
109	analysis.	70
110	Table 7.2: Caption	73
111	Table 7.3: Caption	74

112 List of Figures

113	Figure 2.1: Caption	4
114	Figure 2.2: Caption	7
115	Figure 2.3: Caption	19
116	Figure 2.4: Caption	20
117	Figure 3.1: Caption	23
118	Figure 3.2: Caption	26
119	Figure 4.1: Stages of topo-cluster formation corresponding to each threshold. In (a),	
120	proto-clusters are seeded from cells with adequate signal significance $\zeta_{\text{cell}}^{\text{EM}}$.	
121	The clusters are further merged and split in (b) according to a predefined	
122	cluster growth threshold. The process stops in (c) when all sufficiently	
123	significant signal hits have been matched to a cluster.	34
124	Figure 4.2: Caption	37

KEY TO ABBREVIATIONS

Physical & mathematical quantities

χ^2 chi-squared

ΔR angular distance

η pseudorapidity

E_T transverse energy

E_T^{miss} missing transverse momentum

γ_μ Dirac matrices

I weak isospin

L instantaneous luminosity

μ signal strength

p_T transverse momentum

Particles

b bottom quark

pp proton-proton

$t\bar{t}$ top/anti-top quark

$t\bar{t}t\bar{t}$ four-top-quark

tW single-top

Acronyms

1LOS one lepton, or two leptons of opposite charges

AF3 AtlFast3 fast simulation

ATLAS A Toroidal LHC ApparatuS

BDT boosted decision tree

BSM Beyond the Standard Model

CERN European Organization for Nuclear Research

150 **CMS** Compact Muon Solenoid
151 **CR** control region
152 **ECIDS** Electron Charge ID Selector
153 **EM** electromagnetic
154 **EW** electroweak
155 **FS** full detector simulation
156 **GNN** graph neural network
157 **GUT** Grand Unified Theory
158 **HLT** High-Level Trigger
159 **ID** inner detector
160 **JER** jet energy resolution
161 **JES** jet energy scale
162 **JVT** Jet Vertex Tagger
163 **L1** Level 1
164 **LH** likelihood
165 **LLH** log-likelihood
166 **LO** leading order
167 **LAr** liquid argon
168 **LHC** Large Hadron Collider
169 **ME** matrix element
170 **MS** muon spectrometer
171 **MDT** Monitored Drift Tubes
172 **MET** missing transverse energy
173 **NF** normalization factor
174 **NLO** next-to-leading order
175 **NNLO** next-to-next-to-leading order
176 **NP** nuisance parameter

177 **OP** operating point
 178 **PCBT** pseudo-continuous b -tagging
 179 **PDF** parton distribution function
 180 **POI** parameter of interest
 181 **PS** parton shower
 182 **PV** primary vertex
 183 **QCD** quantum chromodynamics
 184 **QED** quantum electrodynamics
 185 **QFT** quantum field theory
 186 **QmisID** charge mis-identification
 187 **SCT** Semiconductor Tracker
 188 **SF** scale factor
 189 **SM** Standard Model
 190 **SR** signal region
 191 **SSML** two leptons of the same charge, or more than two leptons (multilepton)
 192 **TDAQ** Trigger and Data Acquisition
 193 **TRT** Transition Radiation Tracker
 194 **VEV** vacuum expectation value

Roadmap

1. Finish adding bullets for all sections 06/04

Remaining

- introduction

2. Fill in details 06/13

- Add missing figures

- Add missing bib

3. Finalize analysis

4. String everything together

5. Miscellaneous/logistics (proofreading, review, ATLAS approval, etc.)

6. Submission to the graduate school 07/01

7. Defense 07/15

Chapter 1. Introduction

[1]

1. background and context

2. problem to be solved in thesis

3. aim of analysis: Z' consequences of many BSM theories, searching for Z'

4. hypothesis/research question: searching for Z' in $t\bar{t}t\bar{t}$ SSML channel

5. methodology: data collection - \sqrt{s} analysis regions - \sqrt{s} binned likelihood fit

6. thesis structure:

- ch2: SM/BSM theoretical background

- ch3: LHC/ATLAS experiment

- ch4: samples used in the analysis

- ch5: ATLAS particle reconstruction and identification techniques, and object definitions for the analysis

- ch6: analysis strategy

- ch7: systematic uncertainties affecting the analysis

- ch8: final results

- ch9: summary

Chapter 2. Theoretical Overview

2.1 The Standard Model

The Standard Model of Physics (SM) is currently the most successful formalism to describe the physical world at a microscopic scale.

The SM provides descriptions for all currently known elementary particles and three out of four fundamental forces with the exception of gravity.

2.1.1 Elementary particles

Elementary particles in the SM can be classified into two groups: bosons, consisting of particles following Bose-Einstein statistics with integer spin and fermions, consisting of particles following Fermi-Dirac statistics with half-integer spin

Fermions are the building blocks of composite particles and consequently all known matter, and can be further split into quarks & leptons.

Bosons act as force mediators for all fundamental forces described by the SM. Bosons have two types: a scalar boson with spin 0 and vector gauge bosons with spin 1.

For each elementary particle there also exists a corresponding antiparticle with identical mass and opposite charge (electric or color).

Fermions

Quarks and leptons each has six flavors, grouped into three generations of doublets.

The six quark flavors consist of up (u), down (d), charm (c), strange (s), bottom (b) and top

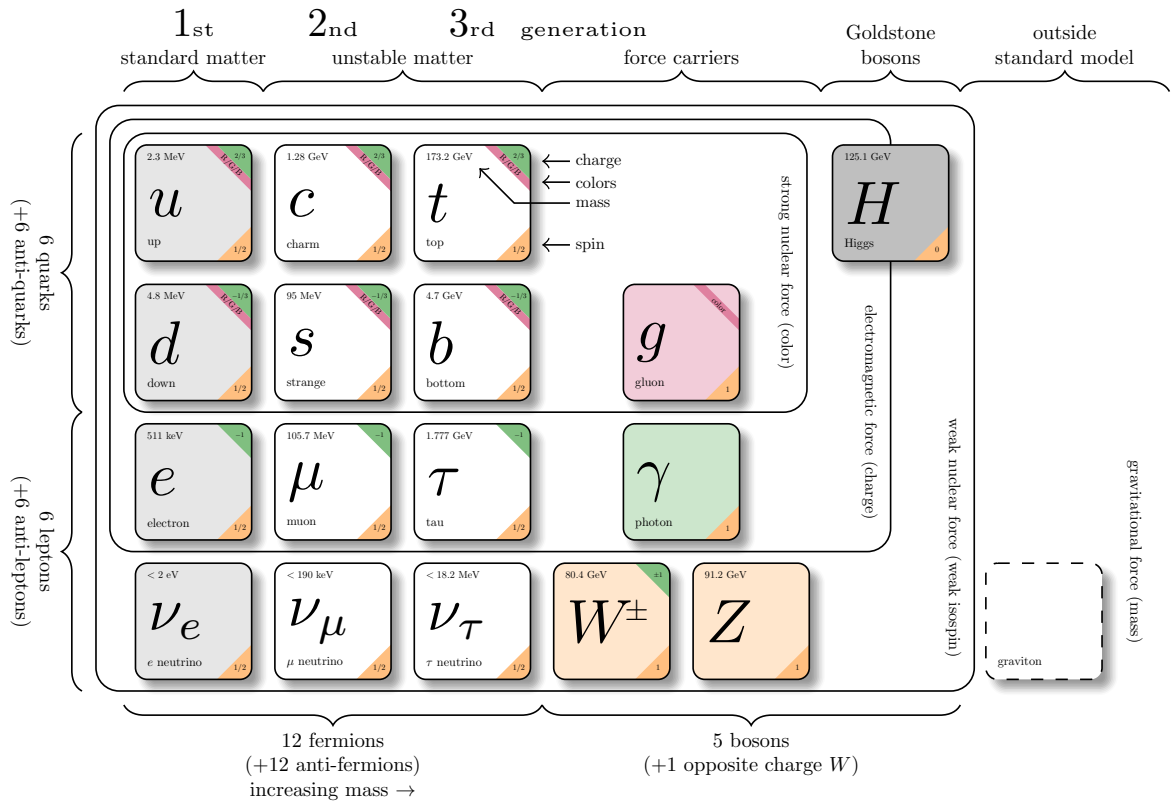


Figure 2.1: Caption[2]

(t) quark flavors in increasing order of mass, forming three doublets (u, d), (c, s) and (t, b).

Each doublet consists of one quark with electric charge of $+2/3$ (u, s, t), and one with charge of $-1/3$ (d, c, b).

Each quark also has a property known as color charge, with possible values of red (R), green (G), blue (B) or antired (\bar{R}), antigreen (\bar{G}), and antiblue (\bar{B}). Color charge follows color confinement rules, which allows only configurations of quarks with neutral color charge to exist in isolation. Neutral charge configurations can be formed from either a set of three colors (R, G, B), a set of a color and its anticolor (q, \bar{q}), or any combination of the two. Consequently, no isolated quark can exist in a vacuum and can only exist in bound states called hadrons.

Quarks are the only elementary particles in the SM that can interact with all four fundamental forces.

The three leptons doublets consist of electron (e), muon (μ), tau (τ) and their respective neutrino flavors: electron neutrino (ν_e), muon neutrino (ν_μ) and tau neutrino (ν_τ)

Charged leptons (e, μ, τ) carry an electric charge of -1 , while their antiparticles carry the opposite charge $+1$ and their corresponding neutrino flavors carrying no charge (charge neutral).

Charged leptons interact with all fundamental forces except the strong force, while neutrinos only interact with the weak force and gravity.

Bosons

The SM classify bosons into two types: one scalar boson with spin 0 known as the Higgs (H) boson, and vector gauge bosons with spin 1 known as gluons (g), photon (γ), W^\pm and Z bosons.

The gluons and photon are massless, while the W^\pm , Z and H are massive.

Each vector gauge boson serves as the mediator for a fundamental force described by the SM.

Gluons are massless mediator particles for the strong interaction between quarks according to quantum chromodynamics (QCD), and carry the color charge in a strong interaction. Each gluon carries a non-neutral color charge out of eight linearly independent color states in the gluon color octet.

Photon is the massless and charge-neutral mediator particle for the electromagnetic interaction following quantum electrodynamics (QED).

The W^\pm and Z bosons are massive mediator particles for the weak interaction, with the W^\pm boson carrying an electric charge of ± 1 while the Z boson is charge neutral.

Other than the vector gauge boson, the only scalar boson in the SM is the Higgs boson which is massive with electric charge of 0.

The Higgs boson does not mediate a fundamental force like vector bosons, but serve to provide the rest mass for all massive elementary particles in the SM through the Higgs mechanism as described in Section 2.21refsec:higgs.

Top quark

As of now, the top quark t is the heaviest particle in the SM with mass of about 173 GeV, compared to the heaviest fermion, the Higgs boson at 125 GeV and the second most massive fermion, the b -quark at about 4.2 GeV. This also gives it the strongest coupling to the Higgs boson and exotic resonances in various proposed BSM models (citations), making the top quark and its processes attractive vehicles with which to probe new physics.

Due to its mass, the top quark has a very short lifetime of 10^{-24} s, and consequently decays

290 before it can hadronize. The top quark decays to a W boson and a b -quark with a branching
 291 ratio of almost 100%, and is assumed to be such for the purpose of this analysis. The W boson
 292 can subsequently decay hadronically or leptonically as shown in Figure 2.2, with branching
 293 ratios of approximately 68% and 32% respectively and with all lepton flavors having similar
 294 ratios assuming lepton universality.

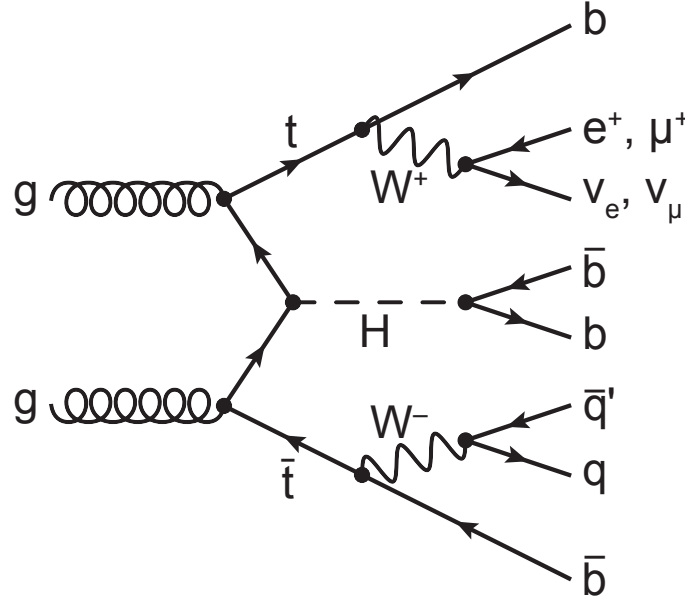


Figure 2.2: $H \rightarrow t\bar{t}$ possible, $t\bar{t}t\bar{t}$ final state[3]

295 2.1.2 Mathematical formalism

296 The SM can be described within the formalism of quantum field theory (QFT) with the
 297 Lagrangian

$$\mathcal{L}_{\text{SM}} = \mathcal{L}_{\text{QCD}} + \underbrace{(\mathcal{L}_{\text{gauge}} + \mathcal{L}_{\text{fermion}} + \mathcal{L}_{\text{Higgs}} + \mathcal{L}_{\text{Yukawa}})}_{\mathcal{L}_{\text{EW}}} \quad (2.1)$$

298 where \mathcal{L}_{QCD} is the QCD term and \mathcal{L}_{EW} is the electroweak (EW) term of the Lagrangian.
 299 QFT treats particles as excitations of their corresponding quantum fields: fermion field ψ ,

300 electroweak boson fields $W_{1,2,3}$ & B , gluon field G_α and Higgs field ϕ .
 301 QFT depends heavily on gauge theory. A quantum field has gauge symmetry if there exists
 302 a continuous gauge transformation that when applied to every point (local gauge transfor-
 303 mation) leaves the field Lagrangian unchanged. The set of gauge transformations of a gauge
 304 symmetry is the symmetry group of the field, which comes with a set of generators, each with
 305 a corresponding gauge field. Under QFT, the quanta of these gauge fields are called gauge
 306 bosons. The SM Lagrangian is gauge invariant under global Poincaré symmetry and local
 307 $SU(3)_C \times SU(2)_L \times U(1)_Y$ gauge symmetry, with the gauge term $SU(3)_C$ corresponding to
 308 the strong interaction and $SU(2)_L \times U(1)_Y$ to the EW interaction.
 309 Global Poincaré symmetry ensures that \mathcal{L}_{SM} satisfies translational symmetry, rotational
 310 symmetry and Lorentz boost frame invariance. By Noether's theorem, gauge symmetries
 311 lead to corresponding conservation laws which leads to conservation of momentum, angular
 312 momentum and energy in the SM.

313 **2.1.2.1 Quantum chromodynamics**

314 QCD is a non-Abelian gauge theory (Yang-Mills theory) describing the strong interaction
 315 between quarks in the SM with the gauge group $SU(3)_C$, where C represents conservation
 316 of color charge under $SU(3)_C$ symmetry.
 317 According to QFT, quarks can be treated as excitations of corresponding quark fields ψ .
 318 Quark fields are invariant under $SU(3)_C$ transformation

$$\psi \rightarrow e^{i\theta(x)T_a}\psi \tag{2.2}$$

where T_a are generators of $SU(3)_C$, represented as $T_a = \lambda_a/2$ with λ_a being the eight Gell-Mann matrices.

The free Dirac Lagrangian

$$\mathcal{L}_0 = \bar{\psi}(i\gamma^\mu\partial_\mu - m)\psi \quad (2.3)$$

is invariant under global $SU(3)$ symmetry, but not under local $SU(3)_C$ symmetry. To establish invariance under local $SU(3)_C$ symmetry, the gauge covariant derivative D_μ is defined so that

$$D_\mu\psi = (\partial_\mu - ig_s G_\mu^a T_a)\psi, \quad (2.4)$$

where $g_s = \sqrt{4\pi\alpha_s}$ is the QCD coupling constant, $G_\mu^a(x)$ are the eight gluon fields that transform under $SU(3)_C$ as

$$G_\mu^a \rightarrow e^{iT_a\theta_a(x)} \left(G_\mu^a + \frac{i}{g_s} \partial_\mu \theta_a(x) \right) e^{-iT_a\theta_a(x)} = G_\mu^a - \frac{1}{g_s} \partial_\mu \theta_a(x) - f_{abc} \theta_b(x) G_\mu^c, \quad (2.5)$$

and T_a are the generators of $SU(3)_C$ defined as $T_a = \lambda_a/2$ with λ_a being the eight Gell-Mann matrices.

Defining the gluon field strength tensor $G_{\mu\nu}^a$ as

$$G_{\mu\nu}^a \equiv \partial_\mu G_\nu^a - \partial_\nu G_\mu^a - g_s f^{abc} G_\mu^b G_\nu^c, \quad (2.6)$$

where f^{abc} are the structure constants of $SU(3)_C$, the gauge invariant QCD Lagrangian is

$$\mathcal{L}_{\text{QCD}} = \bar{\psi}(i\gamma^\mu D_\mu - m)\psi - \frac{1}{4} G_{\mu\nu}^a G_a^{\mu\nu}, \quad (2.7)$$

331 which can be expressed in the form of

$$\mathcal{L}_{\text{QCD}} = \underbrace{-\frac{1}{4}G_{\mu\nu}^a G_a^{\mu\nu}}_{\text{gluon kinematics \& self-interaction}} + \underbrace{\bar{\psi}(i\gamma^\mu\partial_\mu - m)\psi}_{\text{quark kinematics}} + \underbrace{\bar{\psi}^i(g_s\gamma^\mu(T_a)_{ij}G_\mu^a)\psi^j}_{\text{quark-gluon interaction}}. \quad (2.8)$$

332 with i, j being the color indices with integer values from 1 to 3. The noncommutativity
 333 of $SU(3)_C$ gives rise to an additional term consisting of only gluon fields and gluon-gluon
 334 interactions. Additionally, the Lagrangian also forces gluons to be massless to maintain
 335 gauge invariance.

336 2.1.2.2 Electroweak theory

337 The electroweak interaction is the unified description of the weak interaction and electro-
 338 magnetism under the $SU(2)_L \times U(1)_Y$ symmetry group, where L represents the left-handed
 339 chirality of the weak interaction and Y represents the weak hypercharge quantum number.
 340 The quantum number associated with the weak chirality is the weak isospin I . The EW
 341 quantum numbers are connected by the Gell-Mann-Nishijima relation

$$Q = I_3 + Y/2 \quad (2.9)$$

342 where Q is the electric charge and I_3 is the third component of weak isospin I .
 343 Fermions can have either left-handed or right-handed chirality, and can be divided into
 344 left-handed doublets and right-handed singlets

$$\psi_L = \begin{pmatrix} \nu_e \\ e_L \end{pmatrix}, \begin{pmatrix} \nu_\mu \\ \mu_L \end{pmatrix}, \begin{pmatrix} \nu_\tau \\ \tau_L \end{pmatrix}, \begin{pmatrix} u_L \\ d_L \end{pmatrix}, \begin{pmatrix} c_L \\ s_L \end{pmatrix}, \begin{pmatrix} t_L \\ b_L \end{pmatrix} \quad (2.10)$$

$$\psi_R = e_R, \mu_R, \tau_R, u_R, d_R, c_R, s_R, t_R, b_R,$$

345 with the exception of neutrino which can only have left-handed chirality in the SM.

346 Both left-handed and right-handed fermion fields are invariant under $U(1)_Y$ transformation

$$\psi \rightarrow e^{iY\theta(x)/2}\psi. \quad (2.11)$$

347 Similar to QCD, to establish invariance under local $U(1)_Y$ symmetry, the $U(1)_Y$ gauge

348 covariant derivative D_μ is defined as

$$D_\mu\psi = \left(\partial_\mu - ig'\frac{Y}{2}B_\mu\right)\psi \quad (2.12)$$

349 where $B_\mu(x)$ is a vector gauge field that transforms under $U(1)_Y$ as

$$B_\mu \rightarrow B_\mu + \frac{1}{g'}\partial_\mu\theta(x) \quad (2.13)$$

350 and g' is the B_μ coupling constant.

351 Right-handed fermion singlets are not affected by $SU(2)_L$ transformation, so fermion fields

352 transform under $SU(2)_L$ as

$$\psi_L \rightarrow e^{iI_3\vec{\theta}(x)\cdot\vec{\sigma}/2}\psi_L \quad (2.14)$$

$$\psi_R \rightarrow \psi_R.$$

353 where $\vec{\sigma}/2$ are generators of $SU(2)_L$ and $\vec{\sigma}$ are Pauli matrices. In order to preserve local

354 symmetry, the gauge covariant derivative for $SU(2)_L$ is defined as

$$D_\mu\psi_L = \left(\partial_\mu - ig\frac{\sigma_i}{2}W_\mu^i\right)\psi_L \quad (2.15)$$

where $W_\mu^i(x)$ ($i = 1, 2, 3$) are three boson gauge fields that transform under $SU(2)_L$ as

$$W_\mu^i \rightarrow e^{i\frac{\sigma_i}{2}\theta_i(x)} \left(W_\mu^i + \frac{i}{g}\partial_\mu \right) e^{-i\frac{\sigma_i}{2}\theta_i(x)} = W_\mu^i + \frac{2}{g}\partial_\mu\theta_a(x) + \epsilon^{ijk}\theta_j(x)W_\mu^k, \quad (2.16)$$

with g as the gauge coupling constant for W_μ^i , and ϵ^{ijk} as the structure constant for $SU(2)_L$.

The gauge covariant derivative for $SU(2)_L \times U(1)_Y$ can then be written as

$$\begin{aligned} D_\mu\psi_L &= \left(\partial_\mu - ig'\frac{Y_L}{2}B_\mu - ig\frac{\sigma_i}{2}W_\mu^i \right) \psi_L \\ D_\mu\psi_R &= \left(\partial_\mu - ig'\frac{Y_R}{2}B_\mu \right) \psi_R. \end{aligned} \quad (2.17)$$

Similar to QCD, the kinetic term is added by defining field strengths for the four gauge fields

$$\begin{aligned} B_{\mu\nu} &\equiv \partial_\mu B_\nu - \partial_\nu B_\mu \\ W_{\mu\nu}^i &\equiv \partial_\mu W_\nu^i - \partial_\nu W_\mu^i - ge^{ijk}W_\mu^j W_\nu^k. \end{aligned} \quad (2.18)$$

The local $SU(2)_L \times U(1)_Y$ invariant EW Lagrangian can then be expressed as

$$\begin{aligned} \mathcal{L}_{\text{EW}} &= i\bar{\psi}(\gamma^\mu D_\mu)\psi - \frac{1}{4}W_{\mu\nu}^i W_i^{\mu\nu} - \frac{1}{4}B_{\mu\nu}B^{\mu\nu} \\ &= \underbrace{i\bar{\psi}(\gamma^\mu \partial_\mu)\psi}_{\text{fermion kinematics}} - \underbrace{\bar{\psi} \left(\gamma^\mu g' \frac{Y}{2} B_\mu \right) \psi - \bar{\psi}_L \left(\gamma^\mu g \frac{\sigma_i}{2} W_\mu^i \right) \psi_L}_{\text{fermion-gauge boson interaction}} - \underbrace{\frac{1}{4}W_{\mu\nu}^i W_i^{\mu\nu} - \frac{1}{4}B_{\mu\nu}B^{\mu\nu}}_{\text{boson kinematics \& self-interaction}}. \end{aligned} \quad (2.19)$$

Under ≈ 159.5 GeV, the EW symmetry $SU(2)_L \times U(1)_Y$ undergoes spontaneous symmetry breaking into $U(1)_{\text{QED}}$ symmetry, which corresponds to a separation of the weak and electrodynamic forces. This replaces the massless and similarly-behaved EW gauge bosons B_μ and W_μ^i with the EM boson γ and the weak bosons Z/W^\pm . Additionally, electroweak spontaneous symmetry breaking also gives Z and W^\pm masses via the Higgs mechanism, dis-

365 cussed in Section 2.1.2.3. The spontaneous symmetry breaking leads to reparameterization
 366 of B_μ and W_μ^i to $W^\pm/Z/\gamma$ bosons via a specific choice of gauge for the Higgs field

$$\begin{aligned} W_\mu^\pm &\equiv \frac{1}{\sqrt{2}} \left(W_\mu^1 \mp i W_\mu^2 \right) \\ \begin{pmatrix} A_\mu \\ Z_\mu \end{pmatrix} &\equiv \begin{pmatrix} \cos \theta_W & \sin \theta_W \\ -\sin \theta_W & \cos \theta_W \end{pmatrix} \begin{pmatrix} B_\mu \\ W_\mu^3 \end{pmatrix} \end{aligned} \quad (2.20)$$

367 where $\theta_W \equiv \cos^{-1} \left(g / \sqrt{g^2 + g'^2} \right)$ is the weak mixing angle. The boson kinetic term can also
 368 be refactorized to extract cubic (three vertices) and quartic (four vertices) self-interactions
 369 among the gauge bosons [4]. The Lagrangian can then be rewritten as

$$\begin{aligned} \mathcal{L} &= \underbrace{e A_\mu \bar{\psi} (\gamma^\mu Q) \psi}_{\text{electromagnetism}} + \underbrace{\frac{e}{2 \sin \theta_W \cos \theta_W} \bar{\psi} \gamma^\mu (v_f - a_f \gamma_5) \psi Z_\mu}_{\text{neutral current interaction}} \\ &+ \underbrace{\frac{g}{2\sqrt{2}} \sum_{\psi_L} [\bar{f}_2 \gamma^\mu (1 - \gamma_5) f_1 W_\mu^+ + \bar{f}_1 \gamma^\mu (1 - \gamma_5) f_2 W_\mu^-]}_{\text{charged current interaction}} \\ &+ \mathcal{L}_{\text{kinetic}} + \underbrace{\mathcal{L}_{\text{cubic}} + \mathcal{L}_{\text{quartic}}}_{\text{boson self-interaction}} \end{aligned} \quad (2.21)$$

370 where $\gamma_5 = i\gamma^0\gamma^1\gamma^2\gamma^3$ is the chirality projection operator, $a_f = I_3$, $v_f = I_3(1 - 4|Q| \sin^2 \theta_W)$
 371 and f_1, f_2 are up and down type fermions of a left-handed doublet.

372 2.1.2.3 Higgs mechanism

373 So far, the EW bosons are massless, since the mass terms $-m\bar{\psi}\psi$ for fermions and $-mA^\mu A_\mu$
 374 for bosons are not invariant under the EW Lagrangian. The particles must then acquire
 375 mass under another mechanism. The Brout-Engler-Higgs mechanism [5–7] was introduced

376 in 1964 to rectify this issue, and verified in 2012 with the discovery of the Higgs boson [8, 9].

377 The Higgs potential is expressed as

$$V(\phi^\dagger\phi) = \mu^2\phi^\dagger\phi + \lambda(\phi^\dagger\phi)^2 \quad (2.22)$$

378 where μ^2 and $\lambda > 0$ are arbitrary parameters, and the $SU(2)_L$ doublet ϕ is the Higgs field

$$\phi = \begin{pmatrix} \phi^+ \\ \phi^0 \end{pmatrix}, \quad (2.23)$$

379 with complex scalar fields ϕ^+ and ϕ^0 carrying +1 and 0 electric charge respectively. The
380 Lagrangian for a scalar field is

$$\mathcal{L}_H = (\partial_\mu\phi)^\dagger (\partial^\mu\phi) - V(\phi^\dagger\phi). \quad (2.24)$$

381 Since the potential $V(\phi^\dagger\phi)$ is constrained by $\lambda > 0$, the ground state is solely controlled by
382 μ . If $\mu^2 > 0$, the ground state would be $\phi = 0$, and the EW bosons would remain massless.
383 If $\mu^2 < 0$, the ground state would be

$$|\phi|^2 = -\frac{\mu^2}{2\lambda} \equiv \frac{v^2}{\sqrt{2}}, \quad (2.25)$$

384 where v is defined as the vacuum expectation value (VEV). The standard ground state for
385 the Higgs potential without loss of generality can be chosen as

$$\phi(0) = \frac{1}{\sqrt{2}} \begin{pmatrix} 0 \\ v \end{pmatrix}. \quad (2.26)$$

sombrero potential pic

Having $U(1)$ symmetry allows any $-e^{i\theta}\sqrt{\mu^2/\lambda}$ to be a ground state energy for the Higgs Lagrangian. This degeneracy results in spontaneous symmetry breaking of the $SU(2)_L \times U(1)_Y$ symmetry into $U(1)_{\text{QED}}$ symmetry when the Higgs field settles on a specific vacuum state as a result of a perturbation or excitation. The spontaneous symmetry breaking introduces three massless (Nambu-Goldstone) vector gauge boson ξ and a massive scalar boson η , each corresponds to a generator of the gauge group. The bosons can be extracted using the reparameterization [10]

$$\xi \equiv \phi^+ \sqrt{2}, \quad \eta \equiv \phi^0 \sqrt{2} - v, \quad (2.27)$$

such that ξ, η are real fields. The Higgs field now become

$$\phi = \frac{v + \eta + i\xi}{\sqrt{2}} = e^{i\xi \cdot \frac{\sigma}{2v}} \begin{pmatrix} 0 \\ \frac{v + \eta}{\sqrt{2}} \end{pmatrix}. \quad (2.28)$$

Due to $U(1)_{\text{EM}}$ invariance, a unitary gauge with the transformation $\phi \rightarrow \exp(-i\xi \cdot \frac{\sigma}{2v})$ can be chosen to eliminate the massless bosons and incorporate them into the EM and weak bosons through the reparameterization in Equation 2.20. This leaves the massive η which can now be observed as an excitation of the Higgs field and consequently is the Higgs boson h . Using the EW covariant derivative from Equation 2.17, the Higgs Lagrangian around the vacuum state becomes

$$\begin{aligned} \mathcal{L}_H &= (D_\mu \phi)^\dagger (D^\mu \phi) - \mu^2 \left(\frac{v + h}{\sqrt{2}} \right)^2 - \lambda \left(\frac{v + h}{\sqrt{2}} \right)^4 \\ &= (D_\mu \phi)^\dagger (D^\mu \phi) - \frac{1}{2} \mu^2 h^2 - \lambda v h^3 - \frac{\lambda}{4} h^4 - \dots \end{aligned} \quad (2.29)$$

393 The Higgs mass can be extracted from the quadratic term as $m_H = \sqrt{-2\mu^2}$. The kinetic
 394 term in the Lagrangian can be written as

$$\begin{aligned} (D_\mu \phi)^\dagger (D^\mu \phi) &= \frac{1}{2}(\partial_\mu h)^2 + \frac{g^2}{8}(v+h)^2 |W_\mu^1 - iW_\mu^2|^2 + \frac{1}{8}(v+h)^2 (g'W_\mu - gB_\mu)^2 \\ &= \frac{1}{2}(\partial_\mu h)^2 + (v+h)^2 \left(\frac{g^2}{4} W_\mu^+ W^{-\mu} + \frac{1}{8} (g^2 + g'^2) Z_\mu^0 Z^{0\mu} \right). \end{aligned} \quad (2.30)$$

395 Masses for the EW bosons can be extracted from the quadratic terms

$$m_{W^\pm} = \frac{v}{2}g, \quad m_Z = \frac{v}{2}\sqrt{g^2 + g'^2}, \quad m_\gamma = 0. \quad (2.31)$$

396 The fermion mass term $-m\bar{\psi}\psi$ still breaks EW invariance after spontaneous symmetry
 397 breaking. Fermions instead acquire mass by replacing the mass term with a gauge invariant
 398 Yukawa term in the EW Lagrangian for fermions' interactions with the Higgs field [10]

$$\begin{aligned} \mathcal{L}_{\text{Yukawa}} &= -c_f \frac{v+h}{\sqrt{2}} (\bar{\psi}_R \psi_L + \bar{\psi}_L \psi_R) \\ &= - \underbrace{\frac{c_f}{\sqrt{2}} v (\bar{\psi}\psi)}_{\text{fermion mass}} - \underbrace{\frac{c_f}{\sqrt{2}} (h\bar{\psi}\psi)}_{\text{fermion-Higgs interaction}}, \end{aligned} \quad (2.32)$$

399 where c_f is the fermion-Higgs Yukawa coupling. The fermion mass is then $m_f = c_f v / \sqrt{2}$.

400 2.2 Beyond the Standard Model

401 2.2.1 Top-philic vector resonance

402 Many BSM models extend the SM by adding to the SM gauge group additional $U(1)'$ gauge
 403 symmetries, each with an associated vector gauge boson nominally named Z' [11]. In the case

404 of a BSM global symmetry group with rank larger than the SM gauge group, the symmetry
 405 group can break into $G_{\text{SM}} \times U(1)'^n$, where G_{SM} is the SM gauge group $SU(3)_C \times SU(2)_L \times$
 406 $U(1)_Y$ and $U(1)'^n$ is any $n \geq 1$ number of $U(1)'$ symmetries. The existence of additional
 407 vector bosons Z' would open up many avenues of new physics e.g. extended Higgs sectors
 408 from $U(1)'$ symmetry breaking, existence of flavor-changing neutral current (FCNC) effects
 409 in some models, and possible exotic production from heavy Z' decays [11].
 410 Due to the top quark having the largest mass out of all known elementary particles in the SM,
 411 many BSM models [12–15] predict 'top-philic' vector resonances that have much stronger
 412 coupling to the top quark compared to other quarks such that the coupling factors to lighter
 413 quarks are negligible.
 414 The analysis in this thesis attempts to reconstruct a top-philic Z' resonance directly to avoid
 415 dependency on model choice. Previous model-independent BSM $t\bar{t}t\bar{t}$ search [16] in the single-
 416 lepton final state and similar mass ranges showed no significant excess with upper limits on
 417 observed (expected) Z' production cross section between 21 (14) fb to 119 (86) fb depending
 418 on parameter choice. In addition, a simplified color-singlet vector particle model [16, 17] is
 419 employed to study model-dependent interpretations. The interaction Lagrangian assumes
 420 only coupling with the top quark and has the form

$$\begin{aligned}
 \mathcal{L}_{Z'} &= \bar{t}\gamma_\mu (c_L P_L + c_R P_R) t Z'^\mu \\
 &= c_t \bar{t}\gamma_\mu (\cos \theta P_L + \sin \theta P_R) t Z'^\mu,
 \end{aligned}
 \tag{2.33}$$

421 where $c_t = \sqrt{c_L^2 + c_R^2}$ is the top coupling strength, $P_{L/R} = (1 \mp \gamma_5)/2$ are the chirality
 422 projection operators, and $\theta = \tan^{-1}(c_R/c_L)$ is the chirality mixing angle [16]. Expanding

the Lagrangian results in

$$\mathcal{L}_{Z'} = \frac{1}{\sqrt{2}} \bar{t} \gamma_\mu \left[\sin\left(\theta + \frac{\pi}{4}\right) - \left(\sqrt{2} \cos\left(\theta + \frac{\pi}{4}\right)\right) \gamma_5 \right] t Z'^\mu, \quad (2.34)$$

which bears striking resemblance to the EW Lagrangian neutral current interaction term in Equation 2.21, showing the similarity between the Z' and the neutral Z boson which acquires mass as a result of $SU(2)_L \times U(1)_Y$ spontaneous symmetry breaking.

Assuming the Z' mass $m_{Z'}$ is much larger than the top mass ($m_t^2/m_{Z'}^2 \approx 0$), the Z' decay width at leading-order (LO) can be approximated as

$$\Gamma(Z' \rightarrow t\bar{t}) \approx \frac{c_t^2 m_{Z'}}{8\pi}. \quad (2.35)$$

It can be observed that $\Gamma/m_{Z'} \approx c_t^2/8\pi \ll 1$ for $c_t \approx 1$. This suggests a very narrow and well-defined resonance peak, which validates the narrow-width approximation for choice of $c_t = 1$ and supports efforts to directly reconstruct the resonance.

The main production channels for the aforementioned heavy top-philic color singlet Z' are at tree level and loop level, with the one-loop level being the dominant processes. Loop level processes are dependent on the chirality angle θ , where $\theta = \pi/4$ suppresses all but gluon-initiated box subprocesses [16]. To minimize model dependence, only the tree level production was considered and consequently $\theta = \pi/4$ was chosen for this analysis. The Feynman diagrams for tree level production channels are shown in Figure 2.3.

The single-top associated final states tjZ' and tWZ' productions are suppressed by three-body phase space, resulting in smaller cross sections, by a factor of two, compared to the top pair associated final state process $t\bar{t}Z' \rightarrow t\bar{t}t\bar{t}$. Unlike tjZ' and tWZ' which are produced by

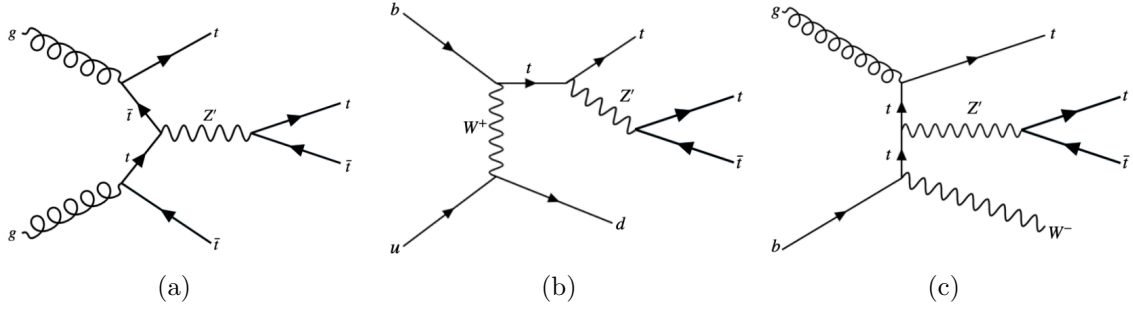


Figure 2.3: tree level Z' production in association with (a) $t\bar{t}$ to 4tops, (b) tj (light quark) to 3tops, (c) tW to 3 tops, derived from top quark final states produced via strong, EW and mixed QCD-EW interactions [16]

EW and mixed QCD-EW interactions respectively, $t\bar{t}t\bar{t}$ production is governed by the strong interaction only which can overpower phase space suppression. Additionally, unlike $t\bar{t}t\bar{t}$ production which is independent of θ , single-top associated processes are minimally suppressed under pure left-handed interaction ($\theta = 0$) and maximally suppressed under pure right-handed interaction ($\theta = \pi/2$).

2.2.2 BSM four-top quark production

The analysis presented in this thesis uses the $t\bar{t}t\bar{t}$ final state signal signature to search for the existence of a heavy BSM resonance that couples strongly to the top quark. Cross section for $t\bar{t}t\bar{t}$ production can be enhanced by many possible BSM models, in particular possible production of a heavy neutral resonance boson X , decaying to a $t\bar{t}$ pair, in association with a $t\bar{t}$ pair in composite Higgs scenarios (citations) or two-Higgs-doublet-model (2HDM!). The $t\bar{t}X$ production mode and consequently $t\bar{t}t\bar{t}$ signal signature can provide a more sensitive channel for searches by avoiding contamination from the large $gg \rightarrow t\bar{t}$ SM background in an inclusive $X \rightarrow t\bar{t}$ search.

Decay modes

The different W boson decay modes shown in Figure 2.2 result in many different final states for $t\bar{t}X/t\bar{t}t\bar{t}$ decay, which can each be classified into one of three channels: all hadronic decays; exactly one lepton or two opposite-sign leptons (1LOS); exactly two same-sign leptons or three or more leptons (SSML). The branching ratio for each channel is shown in Figure 2.4. The all hadronic and 1LOS channels have much larger branching ratios compared to SSML channel but suffer heavily from irreducible $gg \rightarrow t\bar{t}$ background contamination, giving SSML channel better sensitivity at the cost of lower statistics. This is also the targeted channel for the analysis in this thesis.

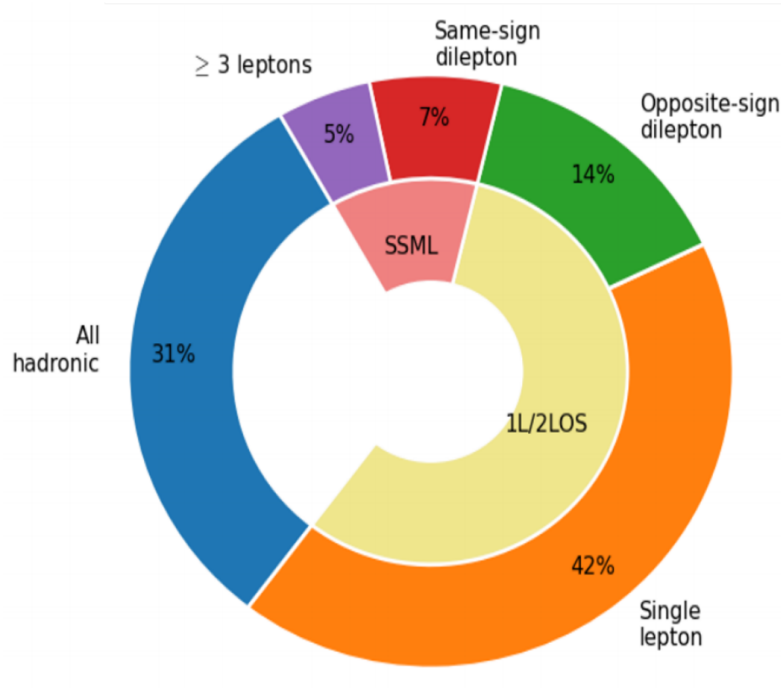


Figure 2.4: Caption

Chapter 3. LHC & ATLAS Experiment

3.1 The Large Hadron Collider

theoretical predictions are tested with experimental data obtained from particle accelerators world's largest accelerator built by CERN situated on the border of Switzerland and France has been operating since xxxx lifetime divided into 3 runs, currently on Run 3 with planned upgrades on the horizon responsible for a number of discoveries aka Higgs, etc.

3.1.1 Overview

[Basic info: location, size, main working mechanism, main detectors, main physics done]
- 27 km circumference, reusing LEP tunnels 175 m below ground level
- 7-13-13.6 TeV center of mass energies for pp collisions
- other than pp, also collides pPb, PbPb at 4 points with 4 main detectors: ATLAS, CMS (general purpose detectors), ALICE (heavy ion physics, ion collisions), LHCb (*b*-physics)

3.1.2 LHC operations

- focuses mainly on pp collisions for this thesis - beams split into bunches of 1.1×10^{11} protons with instantaneous luminosity of up to $2 \times 10^{34} \text{ cm}^{-2}\text{s}^{-1}$
- beam energies ramp up in other accelerators before injection, full ramp up to 6.5 GeV about 20 minutes
(insert full diagram of accelerator chain)
Linac 4: hydrogen atoms, accelerated up to 160 MeV

PSB: H atoms stripped of electrons before injection, accelerated to 2 GeV

PS: 26 GeV, SPS: 450 GeV

LHC: injection in opposite directions, 6.5 TeV per beam

Run 1: 2010-2012, Run 2: 2015-2018, Run 3: 2022-2025, HL-LHC: 2029-?

COM energies: 7 & 8 TeV, 13 TeV, 13.6 TeV, 13.6 & 14 TeV

inbetween periods: long shutdowns (LS1, LS2, LS3)

Physics at the LHC

3.2 The ATLAS detector

multipurpose particle detector with a symmetric cylindrical geometry and a solid angle

coverage of almost 4π

44m long, 25m diameter

inner detector, solenoid/toroid magnet, EM & hadronic calorimeters, muon spectrometer

(insert figure)

right-handed cylindrical system, z-axis follows beamline, azimuthal and polar (0 in the beam direction) angles measured with respect to beam axis.

pseudorapidity $\eta = -\ln \tan(\theta/2)$, approaches $\pm \infty$ along and 0 orthogonal to the beamline

distance $\Delta R = \sqrt{\Delta\eta^2 + \Delta\phi^2}$

transverse energy $E_T = \sqrt{p_T^2 + m^2}$

transverse momentum p_T component of momentum orthogonal to the beam axis $p_T =$

Standard Model Production Cross Section Measurements

Status: October 2023

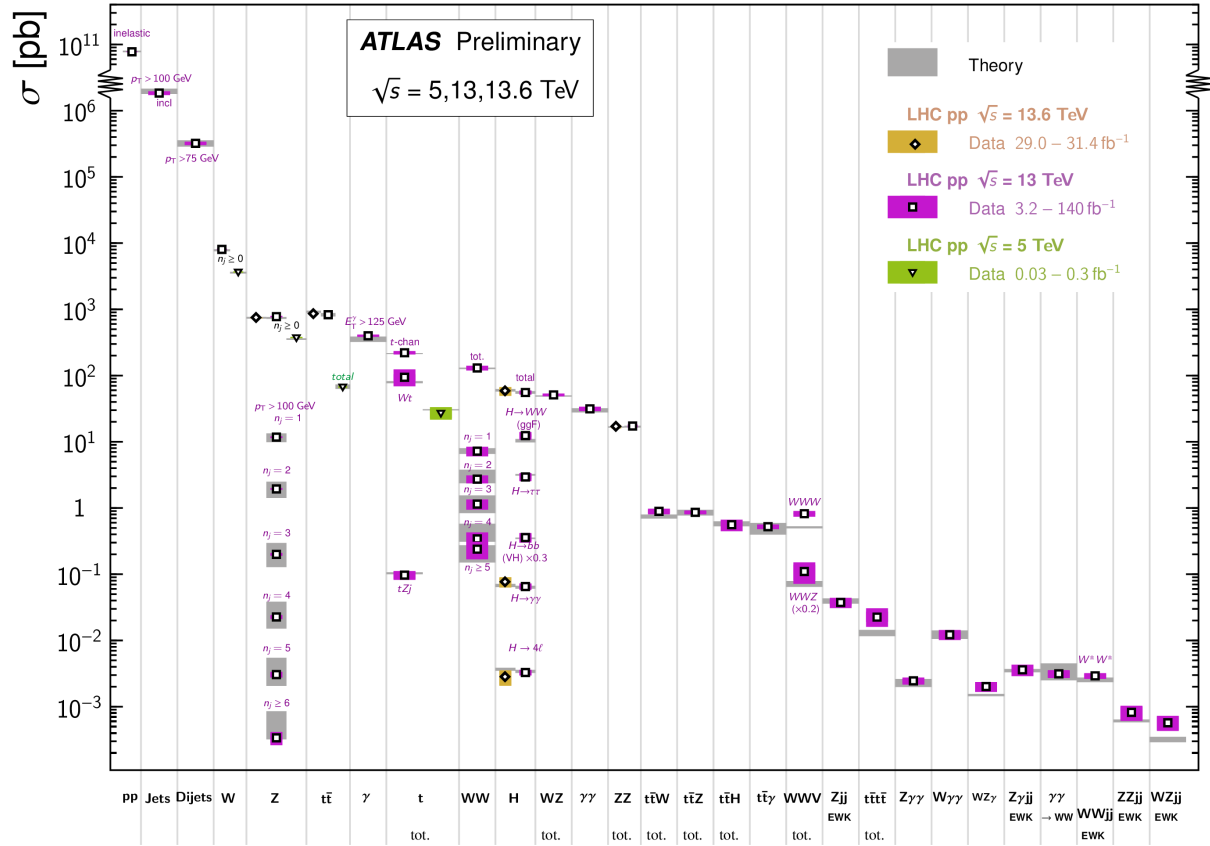


Figure 3.1: Caption [18]

506 $\sqrt{p_x^2 + p_y^2}$

507 3.2.1 Inner detector

508 • measures tracks of charged particles with high momentum resolution ($\sigma_{p_T}/p_T =$
509 $0.05\% \pm 1\%$)

510 • covers particles with $p_T > 0.5$ GeV, $|\eta| < 2.5$

511 pixel detector -> semiconductor tracker -> transition radiation tracker, innermost to
512 outermost

513 • pixel detector:

514 – innermost, 250 μm silicon pixel layers

515 – detects charged particles from electron-hole pair production in silicon

516 – measures impact parameter resolution & vertex identification for reconstruction
517 of short-lived particles

518 – spatial resolution of 10 μm in the $R - \phi$ plane and 115 μm in the z-direction

519 – 80.4m readout channels

520 • sct:

521 – surrounds pixel detector, silicon microstrip layers with 80 μm strip pitch

522 – particle tracks cross 8 strip layers

523 – measures particle momentum, impact parameters, vertex position

524 – spatial resolution of 17 μm in the $R - \phi$ plane and 580 μm in the z-direction

525 – 6.3m readout channels.

• trt:

- outermost, layers of 4 mm diameter gaseous straw tubes with transition radiation material (70% Xe + 27% CO_2 + 3% O_2) & 30 μm gold-plated wire in the center
- tubes 144 cm length in barrel region ($|\eta| < 1$), 37 cm in the endcap region ($1 < |\eta| < 2$), arranged in wheels instead of parallel to beamline)
- gas mixture produces transition radiation when ionized for electron identification
- resolution/accuracy of 130 μm for each straw tube in the $R - \phi$ plane
- 351k readout channels

3.2.2 Calorimeter systems

surrounds the inner detector & solenoid magnet, covers $|\eta| < 4.9$ and full ϕ range. Alternates passive and active material layers. Incoming particles passing through calorimeter produce EM cascades or hadronic showers in passive layer. Energies deposited and convert to electric signals in active layers for readout.

EM calorimeter:

- innermost, lead-LAr detector (passive-active)

- measures EM cascades (bremsstrahlung & pair production) produced by electrons/photons

- divided into barrel region ($|\eta| < 1.475$)

& endcap regions ($1.375 < |\eta| < 3.2$) with transition region ($1.372 < |\eta| < 1.52$) containing extra cooling materials for inner detector

- end-cap divided into outer wheel ($1.372 < |\eta| < 2.5$) & inner wheel ($2.5 < |\eta| < 3.2$)

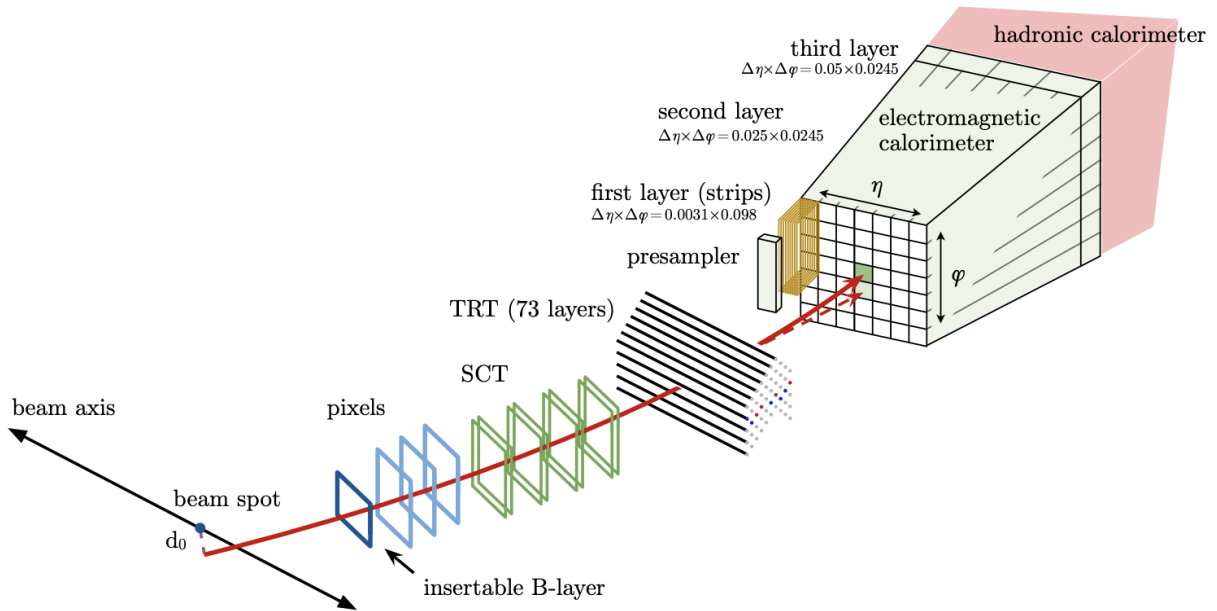


Figure 3.2: Caption [19]

- higher granularity in ID ($|\eta| < 2.5$) range for electrons/photons & precision physics, coarser elsewhere for jet reconstruction & MET measurements
- split into tile calorimeter in barrel region ($|\eta| < 1.0$) & extended barrel region ($0.8 < |\eta| < 1.7$), LAr hadronic end-cap calorimeter (HEC) in end-cap regions ($1.5 < |\eta| < 3.2$) & LAr forward calorimeters (FCal) in $3.1 < |\eta| < 4.9$ range.
- outermost
- measures hadronic showers from inelastic QCD collisions
- thick enough to prevent most particle showers from reaching muon spectrometer
- tile calorimeters: steel-plastic scintillating tiles, readout via photomultiplier tubes
- hec: behind tile calorimeters, 2 wheels per end-cap. copper plates-

LAr. overlap with other calorimeters – fcal: 1 copper module & 2 tungsten modules-LAr. copper optimized for EM measurements, tungsten for hadronic.

3.2.3 Muon spectrometer

- ATLAS outermost layer. measures muon momenta & charge in range $|\eta| < 2.7$
- momentum measured by deflection in track from toroid magnets producing magnetic field orthogonal to muon trajectory
 - large barrel toroids in $|\eta| < 1.4$, strength 0.5 T
 - 2 smaller end-cap toroids in $1.6 < |\eta| < 2.7$, strength 1 T
 - transition region $1.4 < |\eta| < 1.6$, deflection provided by a combination of barrel and end-cap magnets
- chambers installed in 3 cylindrical layers, around the beam axis in barrel region & in planes perpendicular to beam axis in the transition and end-cap regions
- split into high-precision tracking chambers (monitored drift tubes & cathode strip chambers) & trigger chambers (resistive plate chambers & thin gap chambers)
- trigger chambers provide fast muon multiplicity & approximate energy range information with L1 trigger logic

– mdt: $|\eta| < 2.0$

* range $|\eta| < 2.7$, innermost layer * precision momentum measurement

601 ment
 602 * layers of 30 mm drift tubes filled
 603 with 93% *Ar* & 7% *CO*₂, with
 604 a 50 μm gold-plated tungsten-
 605 rhenium wire at the center
 606 * muons pass through tube, ion-
 607 izing gas and providing signals.
 608 Combining signals from tubes
 609 forms track
 610 * maximum drift time from wall
 611 to wire 700 ns
 612 * resolution: 35 μm per chamber,
 613 80 μm per tube
 614 — CSC:
 615 * forward region $2.0 < |\eta| < 2.7$,
 616 highest particle flux and density
 617 region
 618 * multiwire proportional chambers
 619 with higher granularity, filled
 620 with 80% *Ar* & 20% *CO*₂
 621 * shorter drift time than MDT
 622 plus other features making CSC
 623 suitable for high particle density

624 sities and consequently able to
 handle background conditions
 * resolution: 40 μm in bending η -
 plane, 5 mm in nonbending ϕ -
 plane due to coarser cathode seg-
 mentation, per CSC plane

630 – rpc:

633 – tgc:

631 * range $|\eta| < 1.05$

634 * range $1.05 < |\eta| < 2.7$

632 * provide fast meas

635 **3.2.4 Forward detectors**

- 636 • LUCID (LUMinosity measurement using Cherenkov Integrating Detector): ± 17 m from
637 interaction point, measures luminosity using pp scattering in the forward region
- 638 • ALFA (Absolute Luminosity for ATLAS): ± 240 m, measures pp scattering at small
639 angles
- 640 • ZDC (Zero-Degree Calorimeter): ± 140 m, measures centrality in heavy-ion collisions

641 **3.2.5 Magnetic systems**

642 superconducting solenoid & toroid magnets cooled to 4.5 K with liquid helium

643 solenoid: 2.56 m diameter, 5.8 m length, 2 T strength axial magnetic field, encloses inner
644 detector

645 toroid = barrel + endcap toroid x2

646 barrel toroid: 9.2/20.1 m inner/outer diameter, 25.3 m length, 0.5 T strength

647 endcap toroid: 1.65/10.7 m inner/outer diameter, 5 m length, 1 T strength

648 (show magnet system diagram)

649 **3.2.6 Trigger & data acquisition**

650 LHC produces large amount of data (40 MHz with 25 ns bunch crossing), necessitates a way
651 to filter out trash from interesting events

handles online processing, selecting and recording interesting events for further offline processing and more in-depth analyses

- Level-1 (L1) trigger: online, fast hardware-based trigger, reduces to 100 kHz
 - L1 calorimeter triggers (L1Calo): selects high energy objects & MET
 - L1 muon triggers (L1Muon): selects using hit information from RPC & TGC
 - L1 topological trigger (L1Topo): select based on topological selection synthesized using information from L1Calo & L1Muon
 - Central Trigger Processor (CTP): uses L1Calo/Muon/Topo for final L1 trigger decision within $2.5 \mu\text{s}$ latency. Also identify regions of interest in η and ϕ to be processed directly by HLT
- L1 trigger information read out by Front-End (FE) detector electronics then sent to ReadOut Drivers (ROD) for preprocessing and subsequently to ReadOut System (ROS) to buffer
- High-Level Trigger (HLT): offline, software-based trigger, using dedicated algorithms and L1 output as input, reduces to 1 kHz
- Send to storage for analyses after HLT

overall trigger process reduces original collision data rate by a factor of about 10000 after HLT

(show TDAQ diagram)

Chapter 4. Particle Reconstruction & Identification

Activity within the ATLAS detector are recorded as raw electronic signals, which can be utilized by ATLAS reconstruction software to derive physics objects for analysis. This chapter describes the reconstruction and identification of basic objects (e.g. interaction vertices, tracks, topological clusters of energy deposits) and subsequently of complex physics objects i.e. particles and particle signatures.

4.1 Primary reconstruction

4.1.1 Tracks

Charged particles traveling through the ATLAS detector deposit energy in different layers of the ID and MS. The ID track reconstruction software consist of two algorithm chains: inside-out and outside-in track reconstruction [20–22]. specializing in reconstructing tracks from primary and secondary particles respectively.

The inside-out algorithm is primarily used for the reconstruction of primary particles i.e. particles directly produced from pp collisions or decay products of short-lived particles. The process starts by forming space points from seeded hits in the silicon detectors within the pixel & SCT. Hits further away from the interaction vertex are added to the track candidate using a combinatorial Kalman filter [23] pattern recognition algorithm. Track candidates are then fitted with a χ^2 filter [24] and loosely matched to a fixed-sized EM cluster. Successfully matched track candidates are re-fitted with a Gaussian-sum filter (GSF) [25], followed by a

track scoring strategy to resolve fake tracks & hit ambiguity between different tracks [26]. The track candidate is then extended to the TRT to form final tracks satisfying $p_T > 400$ MeV. The outside-in algorithm handles secondary tracks mainly produced from long-lives particles or decays of primary particles by back-tracking from TRT segments, which are then extended inward to match silicon hits in the pixel and SCT to form track reconstruction objects.

4.1.2 Vertices

Vertices represent the point of interaction or decay for particles within the ATLAS detector. Primary vertices (PVs) are defined as the point of collision for hard-scattering pp interactions, while secondary or displaced vertices result from particle decays occurring at a distance from its production point.

Reconstruction of PVs is crucial to accurately profile the kinematic information of an event and form a basis for subsequent reconstruction procedures. Primary vertex reconstruction occurs in two stages: vertex finding and vertex fitting [27]. The vertex finding algorithm uses the spatial coordinates of reconstructed tracks to form the seed for a vertex candidate. An adaptive vertex fitting algorithm [28] then iteratively evaluates track-vertex compatibility to estimate a new best vertex position. Less compatible tracks are down-weighted in each subsequent iteration, and incompatible tracks are removed and can be used for another vertex seed; the process is repeated until no further PV can be found. All reconstructed vertices without at least two matched tracks are considered invalid and discarded.

Secondary vertex reconstruction uses the Secondary Vertex Finder (SVF) algorithm [29] which is primarily designed to reconstruct b - and c -hadrons for flavor tagging purposes.

The SVF aims to reconstruct one secondary vertex per jet and only considers tracks that are matched to a two-track vertex and contained within a p_T -dependent cone around the jet axis. The tracks are then used to reconstruct a secondary vertex candidate using an iterative process similar to the PV vertex fitting procedure.

4.1.3 Topological clusters

One of the main basic reconstruction objects is a topological cluster (topo-cluster) [31], primarily used to reconstruct hadron- and jet-related objects in an effort to extract signal while minimizing electronic effects and physical fluctuations. Topo-clusters also allow for recovery of energy lost through bremsstrahlung or photon conversions.

ATLAS dynamic topological cell clustering algorithms make use of clusters of spatially related cell signals in the calorimeter at the EM scale as basis for reconstruction, while individual cell signals without hits from neighboring cells are considered noise and discarded. Cells with signal-to-noise ratio $\zeta_{\text{cell}}^{\text{EM}}$ passing a primary seed threshold are seeded in as part of a proto-cluster. Neighboring cells satisfying a cluster growth threshold are collected into the proto-cluster. If a cell is matched to two proto-clusters, the clusters are merged. Two or more local signal maxima in a cluster satisfying $E_{\text{cell}}^{\text{EM}} > 500$ MeV suggest the presence of multiple particles in close proximity, and the cluster is split accordingly to maintain good resolution of the energy flow. The process continues iteratively until all cells with $\zeta_{\text{cell}}^{\text{EM}}$ above a principal cell filter level have been matched to a cluster.

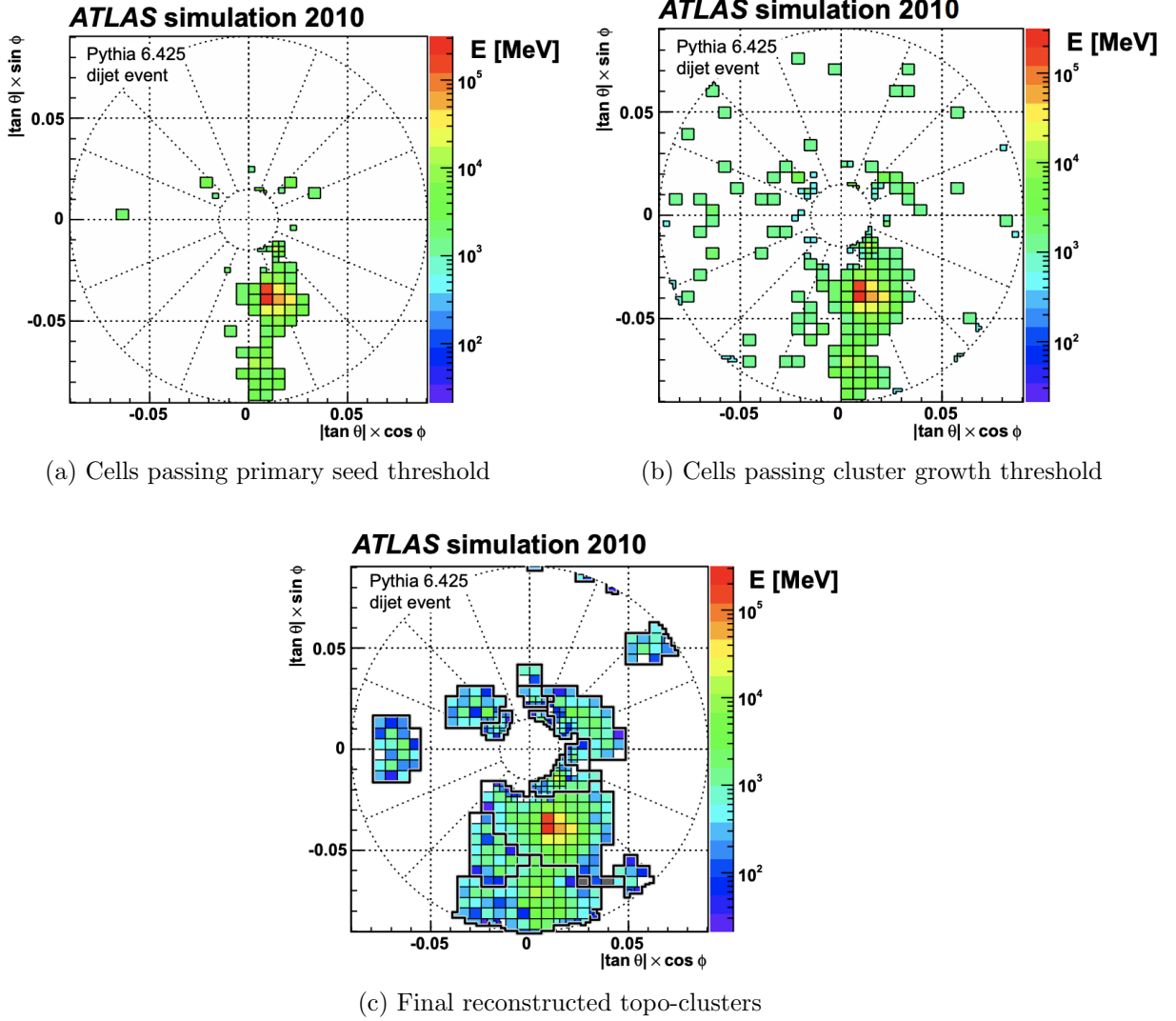


Figure 4.1: Stages of topo-cluster formation corresponding to each threshold. In (a), proto-clusters are seeded from cells with adequate signal significance $\zeta_{\text{cell}}^{\text{EM}}$. The clusters are further merged and split in (b) following a predefined cluster growth threshold. The process stops in (c) when all sufficiently significant signal hits have been matched to a cluster [31]

4.2 Jets

- Quarks, gluons & other non-color-neutral hadrons cannot be observed individually due to QCD color confinement

- A non-color-neutral hadron will almost immediately undergo hadronization producing a cone of color-neutral hadrons also known as a jet

- Jet signals can be used to reconstruct and consequently indirectly observe the original quarks/gluons the jets originated from

- Jet reconstruction:

- PFlow: energy deposited in the calorimeter systems by charged particles is removed and replaced by particle objects created with the remaining energy in the calorimeter and tracks matched to the topo-clusters. (include PFlow graphics)

- anti- k_t algorithms: sequential recombination jet algorithms

- pile-up jets: multiple interactions associated with one bunch crossing in addition to the hard scattering of interest and reconstructed as jets in the final states. Reconstructed pile-up jets can result from Pile-up jets are usually from soft interactions and can be distinguished with JVT algorithm using tracking information from the ID.

- JES/JER calibration: Jet reconstruction at EM scale does not accurately account for energy from QCD interactions and needs to be calibrated to jets reconstructed at particle level. This is done via a MC-based JES calibration sequence and additional JER calibration to match jet resolution in simulation to data using dijet events.

For this analysis, jets are reconstructed using PFlow method with anti- k_t algorithm,

using radius parameter $\Delta R = 0.4$.

JVT applied to reconstructed jets with $p_T < 60$ GeV and $|\eta| < 2.4$.

4.2.1 Flavor tagging

- Classification of hadronic jets is an important task for many LHC analyses especially ones studying final states (Higgs decay/4top)

- Flavor tagging is namely interested in identifying jets containing b -hadrons, c -hadrons, uds -hadrons (light-jets), and hadronic decays from τ .

- Of these, identifying b -jets is of particular interest due to their characteristically long lifetime (≈ 1.5 ps) from decay suppression by CKM factor, with a displaced secondary decay vertex and usually a tertiary vertex from c -hadron decays.

Efficiency calibration

- [32]

- Performance of b -taggers are studied on MC simulated samples. However, the b -tagging efficiency predicted by simulation $\varepsilon_b^{\text{sim}}$ is usually not the same as the efficiency measured in data $\varepsilon_b^{\text{data}}$.

- The correction for the rate of events after applying a b -tagging requirement is calibrated and applied jet by jet in the form of data-to-simulation scale factors $\text{SF} = \varepsilon_b^{\text{data}} / \varepsilon_b^{\text{sim}}$.

- Usage of b -tagger in this analysis is done via five operating points (OPs), corresponding to 60%, 70%, 77%, 85% and 90% b -jet tagging efficiency ε_b in simulated $t\bar{t}$ events in order from loosest to tightest discriminant cut points. - OPs are defined by selection on the tagger output to provide a pre-defined level of ε_b , and act as a variable trade-off between b -tagging efficiency and c -/light-jet rejection i.e. b -jet purity

- A jet is considered b -tagged if it passes the efficiency criteria for a given OP. A pseudo-continuous b -tagging (PCBT) score is defined to summarize the OP criteria a jet passes into a variable. The PCBT score can take integer values between 1 and 6, where a score of 6 means a jet passes all four OP thresholds (passing 65% OP), a score of 2 for jets that pass only the 90% OP, and a score of 1 for jets that don't pass any OP. Additionally, PCBT defines a value of -1 for any jet that does not satisfy b -tagging criteria.

- For this analysis, jets containing b -hadrons are identified and tagged with the GN2v01 algorithm, described in subsection 4.2.1. A jet is considered b -tagged if it passes the 85% WP; this gives the best sensitivity to the signal out of all five possible b -tagging WPs. The b -tagged jet is then assigned a PCBT score accordingly.

bttag optimization table?

GN2 b -tagging algorithm

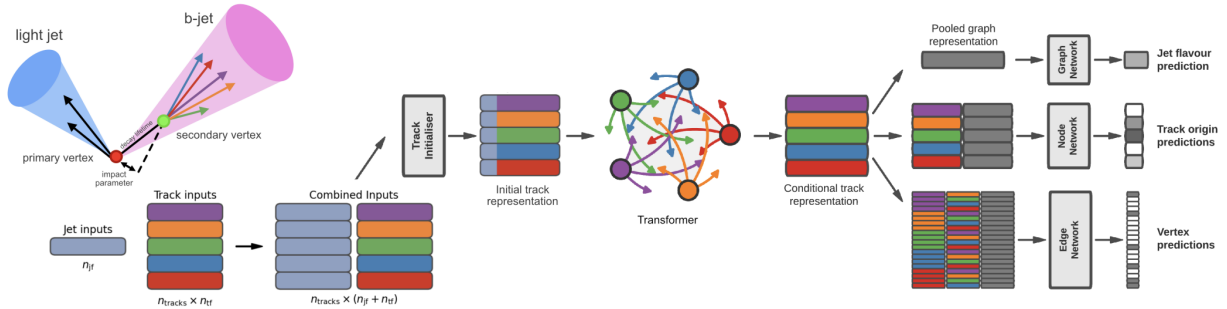


Figure 4.2: Caption [33–35]

- GN2 transformer-based b -tagging algorithm, utilized for analysis of Run 2 and Run 3 data

- GN2 gives a factor of 1.5-4 improvement in experimental applications compared to the

previous convolutional neural network-based standard b -tagging algorithm, DL1d, without dependence on the choice of MC event generator.

- Attention-based architecture, modified to incorporate domain knowledge and additional auxiliary physics objectives: grouping tracks originating from common vertices and prediction of the underlying process for each track

- MC simulated SM $t\bar{t}$ and BSM Z' events from pp collisions were used as training and evaluation samples. In order to minimize bias, both b - and light-jet samples are re-sampled to match c -jet distributions.

- GN2 concatenates 2 jet and 19 track reconstruction variables of up to 40 tracks to form the input feature vector, normalized to zero mean and unit variance.

- The output consists of a jet classification layer of size 4 consisting of p_b , p_c , p_u and p_τ for the probability of each jet being a b -, c -, light- or τ -jet respectively; a track-pairing output layer of size 2, and a track origin classification layer of 7 output categories.

4.3 Leptons

- Lepton reconstruction is concerned mainly with electron and muon construction, since tau decays quickly and can either be reconstructed using jets or light leptons. From here on out lepton will be used mostly to refer to electrons and muons

- Leptons can be classified into two categories: prompt leptons resulting from heavy particle decays, or non-prompt leptons resulting from detector or reconstruction effects, or from b - or c - hadron decays

- Reconstruction of leptons is therefore important to study the underlying physics and suppressing background

4.3.1 Electrons

- [19][36]

- Electrons lose energy interacting with the detector materials via bremsstrahlung. The bremsstrahlung photon can then produce an electron-positron pair which can itself leaves signals in the detector, creating a collimated object that can leave multiple tracks in the ID or EM showers in the calorimeter, all considered part of the same EM topo-cluster.

- Electron signal signature has three characteristic components: localized energy deposits in the calorimeter, multiple tracks in the ID and compatibility between the above tracks and energy clusters in the $\eta \times \phi$ plane. Electron reconstruction in ATLAS follows these steps accordingly - Electron path through the detector is shown in Figure 3.2 - Seed-cluster reconstruction and track reconstruction are performed sequentially in accordance with the iterative clustering algorithm and track reconstruction method respectively, described in section 4.1

- The seed-cluster and track candidate associated with a conversion vertex are then matched to form an electron candidate.

- A reconstructed cluster is expanded from the seed-cluster in either ϕ or η in the barrel or endcap region respectively

- The cluster energy is then calibrated to compute the original electron energy.

Electron identification

- Additional likelihood-based identification selections using ID and EM calorimeter information are implemented to further improve the purity of the reconstructed electrons and photons. These selections also help suppress background from hadronic jet deposits, photon

837 conversions or electrons from heavy-flavor decays.

838 - Three operating points are defined for physics analyses: Loose, Medium and Tight, op-
839 timized for 9 bins in $|\eta|$ and 12 bins in E_T with each corresponding to a fixed efficiency
840 requirement for each bin. The target efficiencies for Loose, Medium and Tight start at 93%,
841 88% and 80% respectively for typical EW processes and increases with E_T
842 Similar to b -tagging OPs, the electron OPs represent a trade-off in signal efficiency and back-
843 ground rejection. The electron efficiency are estimated using tag-and-probe method [19] on
844 samples of $J/\Psi \rightarrow ee$ and $Z \rightarrow ee$ [36].

845 **Electron isolation**

- A characteristic distinction between prompt electrons and electrons from background processes is the relative lack of activity in both the ID and calorimeter within an area of $\Delta\eta \times \Delta\phi$ surrounding the reconstruction candidate

- Electron isolation variables are needed to quantify the amount of activity around the electron candidate.

- Calorimeter-based isolation variables $E_T^{\text{cone}XX}$ is calculated by first summing the energy of topological clusters with barycenters falling within a cone of radius $\Delta R = \sqrt{(\Delta\eta)^2 + (\Delta\phi)^2} = XX/100$ around the direction of the electron candidate.

- The final isolation variable is then obtained by subtracting energy at the core of the cone belonging to the candidate electron from the sum, then applying corrections for energy leakage outside of the core and pile-up effects.

- Similar to calorimeter-based variables, track-based isolation variables $p_T^{\text{varcone}XX}$ are calculated by summing all track p_T within a cone of variable radius ΔR around the electron candidate, minus the candidate's contribution. The cone radius is variable as a function of

p_T

$$\Delta R = \min \left(\frac{10}{p_T[\text{GeV}]}, \Delta R_{\text{max}} \right)$$

with ΔR_{max} being the maximum cone size, to account for the closer proximity of decay products to the electron in high-momentum heavy particle decays.

- Four isolation operating points are implemented to satisfy specific needs by physics analyses: Loose, Tight, HighPtCaloOnly and Gradient. The first three OPs are fixed in isolation variables, while the Gradient OP fixes the isolation efficiency to a p_T dependent function defined as $\varepsilon = 0.1143 \times p_T + 92.14\%$ with p_T in GeV, using $\Delta R = 0.2$ for calorimeter isolation and $\Delta R_{\text{max}} = 0.2$ for track isolation[36].

Electron charge misidentification

[19][37]

Electron charge is determined by the curvature of the associated track. Misidentification of charge can then occur via either an incorrect curvature measurement, or an incorrectly matched track.

The former is more likely for electrons with high p_T due to the small curvature in track trajectories at such scale, while the latter usually results from bremsstrahlung pair-production, creating additional secondary tracks in the vicinity.

Charge misidentification is a crucial irreducible background for analyses with charge selection criteria, and suppression of this background is assisted via a boosted decision tree discriminant known as the Electron Charge ID Selector (ECIDS) [19]. The addition of ECIDS removed 90% of electrons with incorrect charge while selecting 98% of electrons with correct charge from electrons in $Z \rightarrow ee$ events satisfying Medium/Tight identification and Tight

isolation criteria.

4.3.2 Muons

Signature: minimum-ionizing particle leaves tracks in the MS or characteristics energy deposits in the calorimeter

Muons can be reconstructed globally using information from the ID, MS and calorimeters.

Five reconstruction strategies, each corresponding to a muon type:

- Combined (CB): primary ATLAS muon reconstruction method. Muons first reconstructed using MS tracks then extrapolated to include ID tracks (outside-in strategy). A global combined fit is then performed on both MS and ID tracks
- Inside-out combined (IO): Complementary to CB algorithm. Muon tracks are extrapolated from ID to MS, then fitted together with a combined track fit. Useful for muons without good MS information.
- MS extrapolated (ME): ME muons are defined as muons with a MS track that cannot be matched to an ID track using CB method. ME muons allow extension of muon reconstruction acceptance to regions not covered by the ID ($2.5 < |\eta| < 2.7$)
- Segment-tagged (ST): ST muons are ID tracks satisfying tight angular matching criteria to at least one reconstructed local segment in the MDT or CSC chambers when extrapolated to the MS. Used primarily when muons only crossed one layer of MS chambers.
- Calorimeter-tagged (CT): CT muons are ID tracks that when extrapolated through the calorimeter, can be matched to energy deposits consistent with those of a minimum-

ionizing particle. Extends acceptance range to regions in the MS with sparse instrumentation ($|\eta| < 0.1$), with a higher p_T threshold of 5 GeV compared to 2 GeV threshold used by other muon reconstruction algorithms due to large background contamination at the low p_T range of $15 < p_T < 100$ GeV

Muon identification

[38][39]

Reconstructed muons are further filtered by identification criteria to select for high-quality prompt muons for physics analyses. Requirements include number of hits in the MS/ID, track fit properties and compatibility between measurements of the two systems.

Three standard WPs (Loose, Medium, Tight) are defined to better match the needs of different physics analyses concerning prompt muon ID efficiency, p_T resolution and non-prompt muon rejection. Of the three, Medium WP is the default ID WP for ATLAS, by virtue of being optimized in efficiency and purity for a wide range of analyses while minimizing non-prompt rejection and systematic uncertainties[38].

Muon isolation

Muons from heavy particle decays are often produced in an isolated manner compared to muons from semileptonic decays. Muon isolation is therefore an important tool for background rejection in physics analyses

Muon isolation strategies are similar to that of electron in subsection 4.3.1, with track-based and calorimeter-based isolation variables.

Seven isolation WPs are defined to satisfy analyses' needs.

4.4 Missing transverse momentum

[40]

Collisions at the LHC happen along the z -axis of the ATLAS coordination system between two particle beam of equal center-of-mass energy. By conservation of momentum, the sum of transverse momenta of outgoing particles should be zero. A discrepancy between measured momentum and zero would then suggest the presence of undetectable particles, which would consist of either SM neutrinos or some unknown BSM particles. This makes missing transverse momentum ($E_{\text{T}}^{\text{miss}}$) an important observable to reconstruct. Reconstructing $E_{\text{T}}^{\text{miss}}$ utilizes information from fully reconstructed leptons, photons, jets and other matched track-vertex objects not associated with a prompt object (soft signals), defined with respect to the $x(y)$ -axis as

$$E_{x(y)}^{\text{miss}} = - \sum_{i \in \{\text{hard objects}\}} p_{x(y),i} - \sum_{j \in \{\text{soft signals}\}} p_{x(y),j}, \quad (4.1)$$

where $p_{x(y)}$ is the $x(y)$ -component of p_{T} for each particle. The following observables can then be defined:

$$\mathbf{E}_{\text{T}}^{\text{miss}} = (E_x^{\text{miss}}, E_y^{\text{miss}}), \quad (4.2)$$

$$E_{\text{T}}^{\text{miss}} = |\mathbf{E}_{\text{T}}^{\text{miss}}| = \sqrt{(E_x^{\text{miss}})^2 + (E_y^{\text{miss}})^2}, \quad (4.3)$$

$$\phi^{\text{miss}} = \tan^{-1}(E_y^{\text{miss}}/E_x^{\text{miss}}), \quad (4.4)$$

where $E_{\text{T}}^{\text{miss}}$ represents the magnitude of the missing transverse energy vector $\mathbf{E}_{\text{T}}^{\text{miss}}$, and ϕ^{miss} its direction in the transverse plane. Since physics analyses have differing requirements

922 for object selection, the vectorial sum $\mathbf{E}_T^{\text{miss}}$ can be broken down into

$$\mathbf{E}_T^{\text{miss}} = - \underbrace{\sum_{\text{selected electrons}} \mathbf{p}_T^e - \sum_{\text{selected muons}} \mathbf{p}_T^\mu - \sum_{\text{accepted photons}} \mathbf{p}_T^\gamma - \sum_{\text{accepted } \tau\text{-leptons}} \mathbf{p}_T^\tau - \sum_{\text{accepted jets}} \mathbf{p}_T^{\text{jet}}}_{\text{hard term}} - \underbrace{\sum_{\text{unused tracks}} \mathbf{p}_T^{\text{track}}}_{\text{soft term}}. \quad (4.5)$$

923 Two WPs are defined for E_T^{miss} , Loose and Tight [41], with selections on jet p_T and JVT
 924 criteria. The Tight WP is used in this analysis, and reduces pileup dependence of E_T^{miss} by
 925 removing the phase space region with more pileup jets than hard-scatter jets, at the expense
 926 of resolution at low pileup and scale of the reconstructed E_T^{miss} .

927 4.5 Overlap removal

928 Since the reconstruction processes for different objects are performed independently, it is
 929 possible for the same detector signals to be used to reconstruct multiple objects. An overlap
 930 removal strategy to resolve ambiguities; the overlap removal process for this analysis applies
 931 selections listed in Table 4.1 sequentially, from top to bottom.

Table 4.1: Caption [42]

Remove	Keep	Matching criteria
Electron	Electron	Shared ID track, $p_{T,1}^e < p_{T,2}^e$
Muon	Electron	Shared ID track, CT muon
Electron	Muon	Shared ID track
Jet	Electron	$\Delta R < 0.2$
Electron	Jet	$\Delta R < 0.4$
Jet	Muon	$(\Delta R < 0.2 \text{ or ghost-associated}) \ \& \ N_{\text{track}} < 3$
Muon	Jet	$\Delta R < \min(0.4, 0.04 + 10\text{GeV}/p_T^\mu)$

4.6 Object definition

Table 4.2 shows the selections used in this analysis. Each selection comes with associated calibration scale factors to account for discrepancies between data and MC simulation, and are applied multiplicatively to the MC event weights.

Table 4.2: Caption

Selection	Electrons	Muons	Jets
p_T [GeV]	> 15 $p_T(l_0) > 28$	> 15	> 20
$ \eta $	$1.52 \leq \eta < 2.47$ < 1.37	< 2.5	< 2.5
Identification	TightLH pass ECIDS ($ee/e\mu$)	Medium	NNJvt FixedEffPt ($p_T < 60$, $ \eta < 2.4$)
Isolation	Tight_VarRad	PflowTight_VarRad	
Track-vertex assoc.			
$ d_0^{\text{BL}}(\sigma) $	< 5	< 3	
$ \Delta z_0^{\text{BL}} \sin \theta $ [mm]	< 0.5	< 0.5	

Chapter 5. Data & Simulated Samples

5.1 Data samples

LHC Run 2 data collected at $\sqrt{s} = 13$ TeV between 2015-2018

luminosity 140 fb^{-1}

(include uncertainty for Run 2 only)

Triggers used:

Table 5.1: Caption

Trigger	Data period			
	2015	2016	2017	2018
Single electron triggers				
HLT_e24_lhmedium_L1EM20VH	✓	-	-	-
HLT_e60_lhmedium	✓	-	-	-
HLT_e120_lhloose	✓	-	-	-
HLT_e26_lhtight_nod0_ivarloose	-	✓	✓	✓
HLT_e60_lhmedium_nod0	-	✓	✓	✓
HLT_e140_lhloose_nod0	-	✓	✓	✓
Di-electron triggers				
HLT_2e12_lhloose_L12EM10VH	✓	-	-	-
HLT_2e17_lhvloose_nod0	-	✓	-	-
HLT_2e24_lhvloose_nod0	-	-	✓	✓
HLT_2e17_lhvloose_nod0_L12EM15VHI	-	-	-	✓
Single muon trigger				
HLT_mu20_iloose_L1MU15	✓	-	-	-
HLT_mu40	✓	-	-	-
HLT_mu26_ivarmedium	-	✓	✓	✓
HLT_mu50	-	✓	✓	✓

5.2 Monte Carlo samples

Monte Carlo simulated samples are used to estimate signal acceptance before unblinding, profile the physics background for the analysis and to study object optimizations. Simulated samples for this analysis use are generated from ATLAS' generalized MC20a/d/e samples for Run 2, using full detector simulation (FS) and fast simulation (AF3) to simulate detector response.

5.2.1 $t\bar{t}Z'$ signal samples

Signal $t\bar{t}Z'$ samples were generated based on the simplified top-philic resonance model in subsection 2.2.1 where a color singlet vector resonance couples strongly to only top and antitop. Six Z' mass points were utilized for the generation of the signal sample: 1000, 1250, 1500, 2000, 2500 and 3000 GeV. From subsection 2.2.1, the top- Z' coupling c_t is chosen to be 1 for a narrow resonance peak, and the chirality angle θ is chosen to be $\pi/4$ to suppress loop production of Z' . The samples were then generated with MADGRAPH5_AMC@NLO v.3.5.0 [43] at LO with the NNPDF3.1L0 [44] PDF set interfaced with PYTHIA8 [45] using A14 tune and NNPDF2.31o PDF set for parton showering and hadronization. The resonance width is calculated to be 4% for $c_t = 1$.

plots: H_T , nJets, parameter comparison, interference, $m_{t\bar{t}}$ invariant mass

Table 5.2: Summary of all Monte-Carlo samples used in this analysis.

Process	ME Generator	ME Order	ME PDF	PS	Tune	Sim.
Signals						
$t\bar{t}Z'$	MADGRAPH5_AMC@NLO	LO	NNPDF3.1LO	PYTHIA8	A14	FS
$t\bar{t}t\bar{t}$ and $t\bar{t}t$						
$t\bar{t}t\bar{t}$	MADGRAPH5_AMC@NLO	NLO	NNPDF3.0nlo	PYTHIA8	A14	AF3
	MADGRAPH5_AMC@NLO	NLO	MMHT2014 LO	HERWIG7 H7-UE- MMHT		AF3
	SHERPA	NLO	NNPDF3.0nnlo	HERWIG7	SHERPA	FS
$t\bar{t}t$	MADGRAPH5_AMC@NLO	LO	NNPDF2.3lo	PYTHIA8	A14	AF3
$t\bar{t}V$						
$t\bar{t}H$	POWHEGBOX v2	NLO	NNPDF3.0nlo	PYTHIA8	A14	FS
	POWHEGBOX v2	NLO	NNPDF3.0nlo	HERWIG7 H7.2- Default		FS
$t\bar{t}(Z/\gamma^*)$	MADGRAPH5_AMC@NLO	NLO	NNPDF3.0nlo	PYTHIA8	A14	FS
	SHERPA	NLO	NNPDF3.0nnlo	SHERPA	SHERPA	FS
$t\bar{t}W$	SHERPA	NLO	NNPDF3.0nnlo	SHERPA	SHERPA	FS
	SHERPA	LO	NNPDF3.0nnlo	SHERPA	SHERPA	FS
$t\bar{t}$ and Single-Top						
$t\bar{t}$	POWHEGBOX v2	NLO	NNPDF3.0nlo	PYTHIA8	A14	FS
tW	POWHEGBOX v2	NLO	NNPDF3.0nlo	PYTHIA8	A14	FS
$t(q)b$	POWHEGBOX v2	NLO	NNPDF3.0nlo (s) NNPDF3.0nlo 4f (t)	PYTHIA8	A14	FS FS
tWZ	MADGRAPH5_AMC@NLO	NLO	NNPDF3.0nlo	PYTHIA8	A14	FS
tZ	MADGRAPH5_AMC@NLO	LO	NNPDF3.0nlo 4f	PYTHIA8	A14	FS
$t\bar{t}VV$						
$t\bar{t}WW$	MADGRAPH5_AMC@NLO	LO	NNPDF3.0nlo	PYTHIA8	A14	FS
$t\bar{t}WZ$	MADGRAPH	LO	NNPDF3.0nlo	PYTHIA8	A14	AF3
$t\bar{t}HH$	MADGRAPH	LO	NNPDF3.0nlo	PYTHIA8	A14	AF3
$t\bar{t}WH$	MADGRAPH	LO	NNPDF3.0nlo	PYTHIA8	A14	AF3
$t\bar{t}ZZ$	MADGRAPH	LO	NNPDF3.0nlo	PYTHIA8	A14	AF3
$V(VV)+\text{jets}$ and VH						
$V+\text{jets}$	SHERPA	NLO	NNPDF3.0nnlo	SHERPA	SHERPA	FS
$VV+\text{jets}$	SHERPA	NLO LO ($gg \rightarrow VV$)	NNPDF3.0nnlo	SHERPA	SHERPA	FS FS
$VVV+\text{jets}$	SHERPA	NLO	NNPDF3.0nnlo	SHERPA	SHERPA	FS
VH	POWHEGBOX v2	NLO	NNPDF3.0aznlo	PYTHIA8	A14	FS

5.2.2 Background samples

SM $t\bar{t}t\bar{t}$ background

Nominal SM $t\bar{t}t\bar{t}$ sample was generated with MADGRAPH5_AMC@NLO [43] at NLO in QCD with the NNPDF3.0nlo [44] PDF set and interfaced with PYTHIA8.230 [45] using A14 tune [46]. Decays for top quarks are simulated LO with MADSPIN [47, 48] to preserve spin information, while decays for b - and c -hadrons are simulated with EVTGEN v1.6.0 [49]. The renormalization and factorization scales μ_R and μ_F are set to $\sqrt{m^2 + p_T^2}/4$, which represents the sum of transverse mass of all particles generated from the ME calculation [50]. The ATLAS detector response was simulated with AF3. Additional auxiliary $t\bar{t}t\bar{t}$ samples are also generated to evaluate the impact of generator and PS uncertainties as shown in 5.2.

$t\bar{t}W$ background

Nominal $t\bar{t}W$ sample was generated using SHERPA v2.2.10 [51] at NLO in QCD with the NNPDF3.0nnlo [44] PDF with up to one extra parton at NLO and two at LO, which are matched and merged with SHERPA PS based on Catani-Seymour dipole factorization [52] using the MEPS@NLO prescription [53–56] and a merging scale of 30 GeV. Higher-order ME corrections are provided in QCD by the OpenLoops 2 library [57–59] and in EW from $\mathcal{O}(\alpha^3) + \mathcal{O}(\alpha_S^2\alpha^2)$ (LO3 & NLO2) via two sets of internal event weights. An alternative sample with only EW corrections at LO from $\mathcal{O}(\alpha_S\alpha^3)$ (NLO3) diagrams were also simulated with the same settings.

978 $t\bar{t}(Z/\gamma^*)$ background

979 Nominal $t\bar{t}(Z/\gamma^*)$ samples were generated separately for different ranges of dilepton in-
980 variant mass $m_{\ell\ell}$ to account for on-shell and off-shell Z/γ^* production. Sample for $m_{\ell\ell}$
981 between 1 and 5 GeV was produced using MADGRAPH5_AMC@NLO [43] at NLO with
982 the NNPDF3.0nlo [44] PDF set, interfaced with PYTHIA8.230 [45] using A14 tune [46] and
983 NNPDF2.31o PDF set. Sample for $m_{\ell\ell} < 5$ GeV was produced with SHERPA v2.2.10 [51]
984 at NLO using NNPDF3.0nnlo PDF set. To account for generator uncertainty, an alternative
985 $m_{\ell\ell} > 5$ GeV sample was generated with identical settings to the low $m_{\ell\ell}$ sample. The
986 ATLAS detector response was simulated with full detector simulation (FS).

Chapter 6. Analysis Strategy

6.1 Event selection

Events for the analysis first are preselected following a list of criteria to optimize for event quality and background rejection.

The criteria are applied sequentially from top to bottom along with cleaning and veto cuts

1. **Good Run List (GRL)**: data events must be part of a predefined list of suitable runs and luminosity blocks.

2. **Primary vertex**: events must have at least one reconstructed vertex matched to 2 or more associated tracks with $p_T > 500$ MeV.

3. **Trigger**: events must be selected by at least one trigger documented in ??.

4. **Kinematic selection**: events must have exactly two Tight leptons with the same electric charge, or at lease three Tight leptons of any charge. The leading lepton must have $p_T > 28$ GeV, and all leptons must satisfy $p_T > 15$ GeV.

Events are separated into two channels based on the number of leptons: same-sign di-lepton (SS2L) for events with exactly two leptons of the same charge, or multilepton (ML) for events with three or more leptons. The channels are further separated into regions defined in section 6.2 to prepare for analysis.

Further selections are applied based on the lepton flavors present. In the SS2L channel, if both leptons are electrons, the invariant mass m_{ll} must satisfy $m_{ll} < 81$ GeV and $m_{ll} > 101$ GeV to suppress background involving Z -bosons. In the ML channel, the same criteria must be satisfied for every opposite-sign same-flavor pair of leptons in an event.

Event categorization

Simulated events are categorized using truth information of leptons (e/μ) and their originating MC particle (mother-particle).

Each lepton can be classified as either prompt or non-prompt, with non-prompt leptons further categorized for background estimation purposes.

If an event contains only prompt leptons, the event is classified as its corresponding process.

If the event contains one non-prompt lepton, the event is classified as the corresponding type of the non-prompt lepton. If the event contains more than one non-prompt lepton, the event is classified as other.

- **Prompt:** if the lepton originates from $W/Z/H$ boson decays, or from a mother-particle created by a final state photon.

- **Non-prompt:**

- **Charge-flip (e only):** if the reconstructed charge of the lepton differs from that of the first mother-particle.

- **Material conversion (e only):** if the lepton originated from a photon conversion and the mother-particle is an isolated prompt photon, non-isolated final state photon, or heavy boson.

- **γ -conversion (e only):** if the lepton originated from a photon conversion and the mother-particle is a background electron.

- **Heavy flavor decay:** if the lepton originated from a b - or c -hadron.

- **Fake:** if the lepton originated from a light- or s -hadron, or if the truth type of the lepton is hadron.

– **Other**: any lepton that does not belong to one of the above categories.

6.2 Analysis regions

Events are selected and categorized into analysis regions belonging to one of two types: control regions (CRs) enriched in background events, and signal regions (SRs) enriched in signal events. This allows for the examination and control of backgrounds and systematic uncertainties, as well as study of signal sensitivities.

The signal is then extracted from the SRs with a profile LH fit using all regions. The full selection criteria for each region are summarized in Table 6.3

6.2.1 Signal regions

- All events selected for SS2L and 3L signal regions must satisfy the following criteria:

- Contains 6 or more jets, with at least 2 jets b -tagged at the 85% WP
- Scalar sum of the transverse momenta of all leptons and jets $H_T > 500$ GeV
- Dilepton invariant mass $m_{\ell\ell}$ does not coincide with the Z -boson mass range of 81 – 101 GeV

- The SR is further granularized by the number of b -jets and leptons to further study and improve signal sensitivity

Table 6.1: Caption

SR	Selection criteria	
	b -jets	leptons
2b2l	$N_b = 2$	$N_l = 2$
2b3l4l	$N_b = 2$	$N_l \geq 3$
3b2l	$N_b = 3$	$N_l = 2$
3b3l4l	$N_b = 3$	$N_l \geq 3$
4b	$N_b = 4$	

6.2.2 Control regions

Control regions are defined for each background to be enriched in the targeted background events, in order to maximize the targeted background's purity and minimize contamination from other sources within the region.

This helps to constrain and reduce correlation between background normalization factors. Fit variables and selection criteria are determined via optimization studies on CRs to achieve the largest discriminating power possible between the target background and other event types.

$t\bar{t}W$ background CRs

Two types of CRs are defined to estimate the flavor composition and normalization of $t\bar{t}W$ +jets background: CR $t\bar{t}W^\pm$ +jets to constrain flavor composition, and CR 1b(\pm) to constrain jet multiplicity spectrum.

These are further split into CR $t\bar{t}W^\pm$ and CR 1b(\pm) due to the pronounced asymmetry in $t\bar{t}W$ production from pp collisions, with $t\bar{t}W^+$ being produced at approximately twice the rate of $t\bar{t}W^-$. Selections on H_T and N_{jets} to ensure orthogonality to SR

Selections on total charge for each charged W^\pm boson

1064 Fake/non-prompt background CRs

1065 Selection for fake/non-prompt CRs are determined using the `DFCommonAddAmbiguity` (DF-
1066 CAA) variable for reconstructed leptons.

Table 6.2: Caption

DFCAA	Description
-1	No 2nd track found
0	2nd track found, no conversion found
1	Virtual photon conversion candidate
2	Material conversion candidate

1067 Four CRs for three main types of fake/non-prompt backgrounds: virtual photon (γ^*)
1068 conversion, photon conversion in detector material (Mat. Conv.) and heavy flavor decays
1069 (HF).

1070

- 1071 • Low m_γ^* : events with an e^+e^- pair produced from a virtual photon
1072 Selects two same-sign leptons with at least one electron reconstructed as an internal
1073 conversion candidate and neither as with a material conversion candidate ($\text{DFCAA}_{\ell_1(\ell_2)} =$
1074 1 and $\neq 2$)
1075 NF constrained using yield count only.
- 1076 • Mat. Conv.: events with an electron originating from photon conversion within the
1077 detector material.
1078 Selects two same-sign leptons with at least one electron reconstructed as a material
1079 conversion candidate ($\text{DFCAA}_{\ell_1(\ell_2)} = 2$).

NF constrained using yield count only.

- HF e/μ : events with a reconstructed non-prompt lepton from semi-leptonic decays of b - and c -hadrons (heavy flavor decays)

Selects three leptons with at least two electrons/muons, with no lepton reconstructed as a conversion candidate (DFCAA < 0).

NFs constrained by fitting with p_T of the third leading lepton ℓ_3 .

6.2.3 Validation regions

In addition, validation regions are also defined to validate the normalization and modeling of $t\bar{t}Z$ and $t\bar{t}W$ background without being used in the fit.

- $t\bar{t}Z$: Selects events with at least two b -tagged jets, at least four total jets and three leptons with at least one same-flavor opposite-sign lepton pair possessing invariant mass $m_{\ell\ell}$ within the Z -boson mass window of $81 - 101$ GeV

- $t\bar{t}W$: Main charge asymmetric background leaning $t\bar{t}W^+$, validated using the difference in number of positively and negatively charged events $N_+ - N_-$ instead of total number of events.

Selects using CR $t\bar{t}W$ and CR 1b criteria, with one VR not orthogonal to SR and one orthogonal VR with more limited statistics.

6.3 Background estimation

Background events in this analysis consist of SM processes that can result in a $t\bar{t}t\bar{t}$ SSML final state.

Table 6.3: Caption

Region	Channel	N_{jets}	N_b	Other selections	Fitted variable
CR Low m_{γ^*}	SS $e\ell$	[4, 6)	≥ 1	ℓ_1/ℓ_2 is from virtual photon decay $\ell_1 + \ell_2$ not from material conversion	event yield
CR Mat. Conv.	SS $e\ell$	[4, 6)	≥ 1	ℓ_1/ℓ_2 is from material conversion	event yield
CR HF μ	$\ell\mu\mu$	≥ 1	1	$\ell_1 + \ell_2$ not conversion candidates $100 < H_T < 300$ GeV $E_T^{\text{miss}} > 35$ GeV total charge = ± 1	$p_T(\ell_3)$
CR HF e	$e\ell\ell$	≥ 1	1	$\ell_1 + \ell_2$ not conversion candidates $100 < H_T < 275$ GeV $E_T^{\text{miss}} > 35$ GeV total charge = ± 1	$p_T(\ell_3)$
CR $t\bar{t}W^+$	SS $\ell\mu$	≥ 4	≥ 2	$ \eta(e) < 1.5$ for $N_b = 2$: $H_T < 500$ GeV or $N_{\text{jets}} < 6$ for $N_b \geq 3$: $H_T < 500$ GeV total charge > 0	N_{jets}
CR $t\bar{t}W^-$	SS $\ell\mu$	≥ 4	≥ 2	$ \eta(e) < 1.5$ for $N_b = 2$: $H_T < 500$ GeV or $N_{\text{jets}} < 6$ for $N_b \geq 3$: $H_T < 500$ GeV total charge < 0	N_{jets}
CR 1b(+)	SS2L+3L	≥ 4	1	$\ell_1 + \ell_2$ not from material conversion $H_T > 500$ GeV total charge > 0	N_{jets}
CR 1b(-)	SS2L+3L	≥ 4	1	$\ell_1 + \ell_2$ not from material conversion $H_T > 500$ GeV total charge < 0	N_{jets}
VR $t\bar{t}Z$	3L $\ell^\pm\ell^\mp$	≥ 4	≥ 2	$m_{\ell\ell} \in [81, 101]$ GeV	$N_{\text{jets}}, m_{\ell\ell}$
VR $t\bar{t}W + 1b$	SS2L+3L			CR $t\bar{t}W^\pm$ CR 1b(\pm)	N_{jets}
VR $t\bar{t}W + 1b + \text{SR}$	SS2L+3L			CR $t\bar{t}W^\pm$ CR 1b(\pm) SR	N_{jets}
SR	SS2L+3L	≥ 6	≥ 2	$H_T > 500$ GeV $m_{\ell\ell} \notin [81, 101]$ GeV	H_T

1100 Can be divided into two types: reducible and irreducible.
 1101 Reducible background consists of processes that do not result in SSML final state physically,
 1102 but are reconstructed as such due to erroneous detector and reconstruction effects.
 1103 Three main types: charge misidentification (QmisID), fake leptons and non-prompt leptons.
 1104 Estimated using template fitting method to adjust MC predictions via floating normalization
 1105 factors constrained in the CRs.
 1106 Irreducible background consists of SM processes that result in SSML final states physically,
 1107 with all leptons being prompt.
 1108 Main irreducible background considered in this analysis: $t\bar{t}\bar{\ell}$, $t\bar{t}W$, $t\bar{t}Z$, and $t\bar{t}H$ with smaller
 1109 contributions from VV , VVV , VH and rarer processes like $t\bar{t}VV$, tWZ , tZq and $t\bar{t}t$.
 1110 Most irreducible backgrounds are estimated using MC simulations normalized to their the-
 1111 oretical SM cross sections (template fitting), with the exception of $t\bar{t}W$ background due to
 1112 MC mismodeling of the process at high jet multiplicities.
 1113 The $t\bar{t}W$ is instead given four dedicated CRs, and estimated using a data-driven method
 1114 with a fitted function parameterized in N_{jets}
 1115 All CRs and SR are included in the final LH-fit to data.

1116 **6.3.1 Template fitting for fake/non-prompt estimation**

1117 Template fit method is a semi-data-driven approach that estimates fake/non-prompt back-
 1118 ground distributions by fitting the MC kinematic profiles of background processes arising
 1119 from fake/non-prompt leptons to data.
 1120 Each of the four main sources of fake/non-prompt leptons is assigned a free-floating normal-
 1121 ization factor constrained by a CR enriched with the corresponding background. The NFs
 1122 are determined simultaneously with the signal.

- $\text{NF}_{\text{HF } e(\mu)}$: events with one reconstructed non-prompt electron (muon) from heavy flavor decays,
- $\text{NF}_{\text{Mat. Conv.}}$: events with one reconstructed non-prompt electrons from photon conversion in the detector material
- $\text{NF}_{\text{Low } m_{\gamma^*}}$: events with one reconstructed non-prompt electrons in an e^+e^- pair from virtual photon (γ^*) conversion.

6.3.2 Charge misidentification data-driven estimation

The same-sign di-lepton channel in the analysis gives rise to a major background contamination in opposite-sign di-lepton events with one misidentified charge.

Charge misidentification occurs via incorrect track curvature measurements or trident electron contamination from bremsstrahlung, and therefore mainly concerns electrons due to muons' low bremsstrahlung rate and precise curvature information using the ID and MS.

The charge misidentification rates is significant at higher p_T and varies with $|\eta|$ as a proxy for the amount of detector material the electron interacted with, and is consequently estimated in this analysis using a data-driven method with assistance from ECIDS.

The charge flip probability ϵ is estimated using a sample of $Z \rightarrow e^+e^-$ events with additional constraints on the invariant mass m_{ee} to be within 10 GeV of the Z -boson mass.

The Z -boson mass window is defined to be within 4σ to include most events within the peak, and is determined by fitting the m_{ee} spectrum of the two leading electrons to a Breit-Wigner function, resulting in a range of $[65.57, 113.49]$ for SS events and $[71.81, 109.89]$ for OS events.

Background contamination near the peak is assumed to be uniform and subtracted using a sideband method.

1145 Since the Z -boson decay products consist of a pair of opposite-sign electrons, all same-sign
 1146 electron pairs are considered to be affected by charge misidentification.
 1147 Assuming the charge flip probabilities of electrons in an event are uncorrelated, the number
 1148 of events with same-sign electrons N_{ij}^{SS} with the leading electron in the i^{th} 2D bin in $(p_{\text{T}}, |\eta|)$
 1149 and the sub-leading electron in the j^{th} bin can be estimated as

$$N_{ij}^{\text{SS}} = N_{ij}^{\text{tot}}(\epsilon_i(1 - \epsilon_j) + \epsilon_j(1 - \epsilon_i)), \quad (6.1)$$

where N_{ij}^{tot} is the total number of events in the i^{th} and j^{th} bin regardless of charge, and $\epsilon_{i(j)}$ is the charge flip rate in the $i^{\text{th}}(j^{\text{th}})$ bin.

Assuming N_{ij}^{SS} follows a Poisson distribution around the expectation value \bar{N}_{ij}^{SS} , the charge flip rate ϵ can be estimated by minimizing a negative-LLH function parameterized in p_{T} and $|\eta|$,

$$-\ln(\mathcal{L}(\epsilon|N_{\text{SS}})) = -\ln \prod_{ij} \frac{(N_{ij}^{\text{tot}})^{N_{ij}^{\text{SS}}} \cdot e^{-N_{ij}^{\text{tot}}}}{N_{ij}^{\text{SS}}!} \quad (6.2)$$

$$= -\sum_{ij} \left[N_{ij}^{\text{SS}} \ln(N_{ij}^{\text{tot}}(\epsilon_i(1 - \epsilon_j) + \epsilon_j(1 - \epsilon_i))) - N_{ij}^{\text{tot}}(\epsilon_i(1 - \epsilon_j) + \epsilon_j(1 - \epsilon_i)) \right].$$

$$(6.3)$$

1150 The charge flip rate is then calculated separately for SR and CRs with different electron
 1151 definitions (CR Low m_{γ^*} , CR Mat. Conv., CR $t\bar{t}W$) using events satisfying 2LSS kinematic
 1152 selections but with OS electrons, after applying region-specific lepton selections and ECIDS.
 1153 The following weight is applied to OS events to correct for misidentified SS events within

1154 the region:

$$w = \frac{\epsilon_i + \epsilon_j - 2\epsilon_i\epsilon_j}{1 - \epsilon_i - \epsilon_j + 2\epsilon_i\epsilon_j}. \quad (6.4)$$

1155 **6.3.3 $t\bar{t}W$ background data-driven estimation**

1156 - $t\bar{t}W$ represents a major source of irreducible background contamination in SM and BSM
1157 analyses with $t\bar{t}t\bar{t}$ final states.

1158 - Measured cross section for $t\bar{t}W$ background has been consistently higher than predicted
1159 values as seen in previous analyses ($t\bar{t}H/t\bar{t}W$ multilepton [60, 61] and $t\bar{t}t\bar{t}$ [62, 63] analyses)
1160 due to mismodeling, especially at higher N_{jets}
1161 (show postfit $t\bar{t}W$ VR distribution)

1162 - Previously, this was handled by assigning large ad-hoc systematic uncertainties to $t\bar{t}W$
1163 events with 7 or more jets. - A semi-data-driven method originally employed in the R-parity-
1164 violating-supersymmetry search [64] was used to mitigate this problem. - This method was
1165 shown to be effective in the SM $t\bar{t}t\bar{t}$ observation analysis [63] by improving $t\bar{t}W$ modeling
1166 especially in the showering step and switching $t\bar{t}W$ systematic uncertainties from predomi-
1167 nantly modeling to statistical.

1168 - MC kinematic distributions for $t\bar{t}W$ are applied with correction factors obtained from a
1169 fitted function parameterized in N_{jets} .

1170 - The function describes scaling patterns for QCD [65] can be represented by ratio of suc-
1171 cessive exclusive jet cross-sections

$$R_{(n+1)/n} = e^{-b} + \frac{\bar{n}}{n+1} = a_0 + \frac{a_1}{1 + (j-4)}, \quad (6.5)$$

1172 where n is the number of jets in addition to the hard process, j is the inclusive number of
 1173 jets, and \bar{n} is the expectation value for the Poisson distribution for exclusive jet cross-section
 1174 at jet multiplicity n , described as $P_n = \sigma_n / \sigma_{\text{tot}}$.

1175 - Same-sign di-lepton $t\bar{t}W$ events dominate the $t\bar{t}W$ background and produce 4 jets in the
 1176 matrix element at tree level for the hard process, so n is defined starting from 5 jets and j
 1177 is defined as inclusive number of jets with 4 or more jets, or $j \equiv n + 4$.

1178 - The two terms in the equation correspond respectively to staircase and Poisson scaling
 1179 between successive multiplicity cross sections, defined as constant ratios e^{-b} and ratios be-
 1180 tween Poisson probability for $n + 1$ and n jets. Staircase scaling is sensitive to events with
 1181 high jet multiplicity, while Poisson scaling is sensitive to events with low jet multiplicity [65].

1182 - The scaling pattern can then be re-parameterized in a_0 and a_1 to obtain the $t\bar{t}W$ yield at
 1183 j'

$$\text{Yield}_{t\bar{t}W(j')} = \text{Yield}_{t\bar{t}W(j=4)} \times \prod_{j=4}^{j'-1} \left(a_0 + \frac{a_1}{1 + (j - 4)} \right) \quad (6.6)$$

1184 where j' is defined as $j' \equiv j + 1$ with $j \geq 4$ since the parameterization starts at the 4th jet.
 1185 The $t\bar{t}W$ yield at the 4-jet bin can be represented by a normalization factor applied to $t\bar{t}W$
 1186 MC simulation as $\text{Yield}_{t\bar{t}W(j=4)} = \text{NF}_{t\bar{t}W(j=4)} \times \text{MC}_{j=4}$.

1187 To account for the disparity in $t\bar{t}W^+$ and $t\bar{t}W^-$ cross-section, assuming the scaling is the
 1188 same for both processes, $\text{NF}_{t\bar{t}W(j=4)}$ can be further split into $\text{NF}_{t\bar{t}W^+(j=4)}$ and $\text{NF}_{t\bar{t}W^-(j=4)}$.
 1189 Both NFs are left free-floating to constrain $t\bar{t}W$ yields at the 4-jet bin in CR 1b(+) and CR
 1190 1b(-).

1191 The final N_{jets} -parameterized function can then be represented by $\text{NF}_{t\bar{t}W(j')}$ as

$$\text{NF}_{t\bar{t}W(j')} = \left(\text{NF}_{t\bar{t}W^+(j=4)} + \text{NF}_{t\bar{t}W^-(j=4)} \right) \times \prod_{j=4}^{j'-1} \left(a_0 + \frac{a_1}{1 + (j - 4)} \right). \quad (6.7)$$

1192 This normalization is calculated and applied separately for each sub-sample of $t\bar{t}W^+$ and
1193 $t\bar{t}W^-$ in an N_{jets} bin for $4 \leq N_{\text{jets}} < 10$.

1194 Due to small contributions in the CRs, events with $N_{\text{jets}} < 4$ and $N_{\text{jets}} \geq 10$ are not
1195 normalized with this scheme.

1196 Instead, $N_{\text{jets}} < 4$ $t\bar{t}W$ events are fitted by propagating normalization in the 4-jet bin
1197 without additional shape correction. The correction factor for $t\bar{t}W$ events with $N_{\text{jets}} \geq$
1198 10 is obtained by summing up the overflow from $N_{\text{jets}} = 10$ to $N_{\text{jets}} = 12$, described as
1199 $\sum_{j'=10}^{12} \prod_{j=4}^{j'-1} \left(a_0 + \frac{a_1}{1+(j-4)} \right)$. Events with $N_{\text{jets}} \geq 13$ are negligible and thus not included
1200 in the sum.

1201 Control region definitions

1202 Four control regions CR $t\bar{t}W^+$, CR $t\bar{t}W^-$, CR 1b(+), CR 1b(-) are constructed to fit
1203 $\text{NF}_{t\bar{t}W^\pm(j=4)}$ and the scaling parameters a_0 , a_1 for the $t\bar{t}W$ background, as well as vali-
1204 dating the parameterization.

1205 Events in CR $t\bar{t}W^\pm$ are required to contain at least two b -tagged jets similar to the SR to
1206 determine the $t\bar{t}W$ normalization within an SR-related phase space. Orthogonality with SR
1207 is satisfied by requiring $H_{\text{T}} < 500$ GeV or $N_{\text{jets}} < 6$ when $N_b = 2$, and $H_{\text{T}} < 500$ GeV when
1208 $N_b \geq 3$.

1209 The remaining CR 1b(\pm) require events to have $H_{\text{T}} > 500$ GeV and at least four jets to
1210 encompass events with high N_{jets} , which can be used to determine the $t\bar{t}W$ jet multiplic-

1211 ity spectrum for fitting $a_{0,1}$. The selection criteria also include exactly one b -tagged jet to
 1212 maintain orthogonality with SR. Assuming the $t\bar{t}W$ jet multiplicity distribution is similar
 1213 across different N_b , a fitted N_{jets} distribution in CR 1b(\pm) can be used to describe the $t\bar{t}W$
 1214 parameterization at higher N_{jets} . The full selection criteria for all four regions are shown in
 1215 ??

1216

1217 Validating the $t\bar{t}W$ parameterization in Equation 6.7 makes use of the unique charge
 1218 asymmetry in $t\bar{t}W$ production that's not present in other background or signal processes.
 1219 The number of events with all negatively charged leptons is subtracted from that of events
 1220 with all positively charged leptons, which cancels out charge symmetric events and leaves
 1221 the $t\bar{t}W$ background. Validation is done via a statistical-only (stat-only) fit to the $t\bar{t}W$ MC
 1222 prediction in CR 1b(\pm).

Chapter 7. Systematic Uncertainties

(nuisance parameters)

- Heavy pruning, 10% on shape and normalization pruning (to fit timeline?)

7.1 Experimental uncertainties

Instrumental & minor:

- uncertainty on the integrated luminosity of the 2015-2018 Run 2 data set is 0.83%, obtained by the LUCID-2 detector for the primary luminosity measurements complemented by the ID and calorimeters

- Pile-up modeling in MC was calibrated to data through pile-up reweighting, resulting in a set of calibration SFs and associated uncertainties.

In general, calibrating MC simulations to match performance in data incurs uncertainties associated with the MC-to-data scale factors obtained from the calibration, which are in turn propagated to observables in the analysis.

7.1.1 Leptons

The trigger/reconstruction/ID/isolation efficiencies of electrons and muons (with separate systematic and statistical components for muon) differ between MC simulation and data, and require correction in the form of SFs with its associated uncertainties.

Similarly, electron and muon energy-momentum scale and resolution also incur uncertainties from MC-to-data correction, calculated by varying scale and resolution during simulations.

Muons have additional uncertainties for charge-dependent and charge-independent momen-

tum scale, and detector-specific (ID, MS, CB) track resolution.

The charge identification/ECIDS efficiency also gives rise to an additional uncertainty component.

7.1.2 Jets

Experimental uncertainties on jets are dominated by flavor tagging-related uncertainties, with subleading contributions from jet energy scale/resolution (JES/JER) and NNJvt calibration.

Jet energy scale

JES and its associated uncertainties are determined using data from test-beam and LHC collisions and MC simulated samples, decomposed into uncorrelated components:

- Effective nuisance parameters (NPs): 15 p_T -dependent uncertainty components in total measured in situ, grouped based on their origin (2 detector-related, 4 modeling-related, 3 mixed, 6 statistical-related)
- η intercalibration: 6 total components (1 modeling-related, 4 non-closure and 1 statistical-related) associated with the correction of the forward jets' ($0.8 \leq |\eta| < 4.5$) energy scale to that of the central jets ($|\eta| < 0.8$).
- Flavor composition/response: 2 components for relative quark-gluon flavor compositions in background and signal samples, and 2 components for uncertainty in responses to gluon-initiated versus quark-initiated jets

- Pile-up subtraction: 4 components, two for uncertainty in μ (`OffsetMu`) and N_{PV} (`OffsetNPV`) modeling, one for residual p_{T} -dependency (`PtTerm`) and one for topology dependence on the per-event p_{T} density modeling (`RhoTopology`)
- Punch-through effect treatment: two terms (AF3 fast simulation and full detector simulations) for GSC punch-through jet response correction between data and MC.
- Non-closure: one term to account for difference between AF3-simulated samples and full detector simulations.
- High- p_{T} single-particle response: one term for response to high- p_{T} jets from single-particle and test-beam measurements
- b -jets response: one term for uncertainty in the response to b -jets

Jet energy resolution

JER measured separately in data and MC simulations using in situ techniques as a function of p_{T} and η for a given jet. Associated uncertainties are defined as quadratic difference between data and MC simulations.

This analysis uses the full JER uncertainty set provided for Run 2 searches with 14 total components: 12 effective NPs and 2 for difference between data and MC simulation, separately for AF3 and FS.

Jet vertex tagging

JVT associated uncertainty is obtained by varying the JVT efficiency correction SFs within their range of uncertainty. This uncertainty accounts for remaining contamination from pile-up jets after applying pile-up suppression and MC generator choice.

Flavor tagging

SFs for b -jets tagging efficiencies and c -/light-jets mis-tagging rates are obtained as a function of p_T for b -/ c -/light-jets and PCB scores. The covariance matrix of systematic and statistical uncertainties is diagonalized and reduced in dimensions using principle component analysis (PCA), resulting in a set of orthogonal NPs: 85 for b -jets, 56 for c -jets and 42 for light-jets.

7.1.3 Missing transverse energy

Uncertainties for E_T^{miss} arise from possible miscalibration of its soft-track component, and are estimated using data-MC comparison of the p_T scale and resolution between the hard and soft E_T^{miss} terms. These uncertainties are represented by three independent terms: one for scale uncertainty and two resolution uncertainties for the parallel and perpendicular components.

7.2 Modeling uncertainties

7.2.1 Signal and irreducible background uncertainties

- scale variations - 6-point variation method, varying μ_R & μ_F vs central values to cover missing higher-order QCD corrections (signal & all major irreducible background)

$(\mu_R, \mu_F) = (0.5, 0.5), (0.5, 1), (1, 0.5), (1, 2), (2, 1), (2, 2)$ - pdf uncertainty: flat 1% for $t\bar{t}Z'$, $t\bar{t}t\bar{t}$, $t\bar{t}Z$, $t\bar{t}H$, envelope of differences between nominal vs. other pdf choices for $t\bar{t}t$

$t\bar{t}Z'$ signal

- parton distribution function: 1%

Table 7.1: Summary of the experimental systematic uncertainties considered in this analysis.

Systematic uncertainty	Terms	Scale [%]
Event		
Luminosity	1	0.83
Pile-up reweighting	1	$\mathcal{O}(1) \sim \mathcal{O}(10)$
Electrons		
Trigger efficiency	1	$\mathcal{O}(10^{-2}) \sim \mathcal{O}(10^{-1})$
Reconstruction efficiency [†]	1	$\mathcal{O}(10^{-1}) \sim \mathcal{O}(1)$
Identification efficiency [†]	1	$\mathcal{O}(10^{-1}) \sim \mathcal{O}(1)$
Isolation efficiency [†]	1	$\mathcal{O}(10^{-1}) \sim \mathcal{O}(1)$
Energy scale	1	$\mathcal{O}(10^{-2}) \sim \mathcal{O}(10^{-1})$
Energy resolution	1	$\mathcal{O}(10^{-2}) \sim \mathcal{O}(10^{-1})$
Charge identification (ECIDS) efficiency [†]	1	$\mathcal{O}(10^{-1}) \sim \mathcal{O}(1)$
Muons		
Trigger efficiency (stat/sys)	2	$\mathcal{O}(10^{-1}) \sim \mathcal{O}(1)$
Track-to-vertex association efficiency (stat/sys)	2	$\mathcal{O}(10^{-2}) \sim \mathcal{O}(10^{-1})$
Reconstruction/identification efficiency (stat/sys)	2	$\mathcal{O}(10^{-1}) \sim \mathcal{O}(1)$
Low- p_T (< 15 GeV) reconstruction/identification efficiency (stat/sys)	2	$\mathcal{O}(10^{-1}) \sim \mathcal{O}(1)$
Isolation efficiency (stat/sys)	2	$\mathcal{O}(10^{-1}) \sim \mathcal{O}(1)$
Charge-independent momentum scale	1	$\mathcal{O}(10^{-2}) \sim \mathcal{O}(10^{-1})$
Charge-dependent momentum scale	4	$\mathcal{O}(10^{-2}) \sim \mathcal{O}(10^{-1})$
Energy resolution (CB)	1	$\mathcal{O}(10^{-2}) \sim \mathcal{O}(10^{-1})$
Energy resolution (ID & MS)*	2	$\mathcal{O}(10^{-2}) \sim \mathcal{O}(10^{-1})$
Jets		
JES effective NP	15	$\mathcal{O}(10^{-2}) \sim \mathcal{O}(1)$
JES η intercalibration	3	$\mathcal{O}(10^{-1}) \sim \mathcal{O}(1)$
JES flavor composition	2	$\mathcal{O}(10^{-1}) \sim \mathcal{O}(1)$
JES flavor response	1	$\mathcal{O}(10^{-1}) \sim \mathcal{O}(1)$
JES pile-up	4	$\mathcal{O}(10^{-1}) \sim \mathcal{O}(10)$
JES punch-through (FS/AF3*)	2	$< \mathcal{O}(10^{-2})$
JES non-closure	1	$\mathcal{O}(10^{-2}) \sim \mathcal{O}(10^{-1})$
JES high- p_T single particle	1	$< \mathcal{O}(10^{-2})$
JES b -jet response	1	$\mathcal{O}(10^{-1}) \sim \mathcal{O}(1)$
JER effective NP	12	$\mathcal{O}(10^{-1}) \sim \mathcal{O}(1)$
JER data/MC (FS/AF3*)	2	$\mathcal{O}(10^{-1}) \sim \mathcal{O}(1)$
JVT efficiency	1	$\mathcal{O}(10^{-1}) \sim \mathcal{O}(1)$
GN2v01 b -tagging efficiency (b -jets)	85	$\mathcal{O}(10^{-2}) \sim \mathcal{O}(1)$
GN2v01 b -tagging efficiency (c -jets)	56	$\mathcal{O}(10^{-2}) \sim \mathcal{O}(1)$
GN2v01 b -tagging efficiency (light-jets)	42	$\mathcal{O}(10^{-2}) \sim \mathcal{O}(1)$
E_T^{miss}-Terms		
Track-based soft term for transversal resolution	1	$\mathcal{O}(10^{-2}) \sim \mathcal{O}(10^{-1})$
Track-based soft term for longitudinal resolution	1	$\mathcal{O}(10^{-2}) \sim \mathcal{O}(10^{-1})$
Track-based soft term for longitudinal scale	1	$\mathcal{O}(10^{-2}) \sim \mathcal{O}(10^{-1})$

1304 **SM $t\bar{t}t\bar{t}$ background**

- 1305 - cross section: 20% from NLO prediction in QCD+EW
- 1306 - generator uncertainty: madgraph5_amc@nlo (nominal) vs sherpa 2.2.10
- 1307 - parton shower uncertainty: pythia8 (nominal) vs herwig7

1308 **SM $t\bar{t}t$ background**

- 1309 - cross section: 30% from NLO prediction in QCD+EW
- 1310 - additional b -jets: 50% for $t\bar{t}t$ events with 4+ truth b -jets

1311 **$t\bar{t}W$, $t\bar{t}Z$, $t\bar{t}H$ background**

- 1312 - cross section: $t\bar{t}Z$ 12%, $t\bar{t}H$ 10% (from CERN yellow report)
- 1313 no cross-section and pdf uncertainties for $t\bar{t}W$ since normalizations and jet multiplicity spec-
- 1314 trum are estimated with data-driven method
- 1315 - parton shower uncertainty: $t\bar{t}H$ powhegbox+pythia8 (nominal) vs powhegbox+herwig7
- 1316 - additional b -jets: events with additional HF jets can contaminate SR and are challenging
- 1317 to model w/ MC - 50% for events with an additional truth b -jet not from top-quark decay,
- 1318 additional 50% for 2 or more
- 1319 - generator uncertainty **table?**
- 1320 • $t\bar{t}W$ - sherpa (nominal) vs madgraph5_amc@nlo
- 1321 • $t\bar{t}Z$ - madgraph5_amc@nlo (nominal) vs sherpa 2.2.10
- 1322 • $t\bar{t}H$ - powheg8/PhPy8 (nominal) vs powheg8/PhPy8 pthard

Other backgrounds

- $t(\bar{t})X$: cross section 30%
- VV : cross section (STDM-2018-03) uncorrelated 20%/50%/60% for events with 3-
/4/5+ jets; events with 1+ truth b -jets not from top decay 50%
- $t\bar{t}VV, VVV, VH$: cross section 50%; additional b -jets same as VV

7.2.2 Reducible background uncertainties

- Electron charge misidentification background:
- Material and internal (low γ^*) conversion background: estimated based on data/MC differences in a region enriched with $Z \rightarrow \ell^+ \ell^- \gamma$; 30% & 21% for material & internal conversion
- Heavy-flavor non-prompt lepton background: estimated based on data/MC differences in CR/SR distributions, ranging from 20-100%
- Light-flavor decays and other fake/non-prompt background: Conservative normalization uncertainty of 100% for light-flavor non-prompt lepton background (ATLAS-CONF-2019-045), 30% for normalization of all other fake backgrounds.
- +HF: contaminates SR phase space with large b -jet multiplicity, estimated from data/MC discrepancy, 30% for events with

Table 7.2: Caption

Systematic uncertainty	Terms	Scale [%]
$t\bar{t}Z'$ modeling		
Renormalization & factorization scale		
PDF		
SM $t\bar{t}t\bar{t}$ modeling		
Cross-section		
Renormalization & factorization scale		
PDF		
Generator choice		
Parton shower model		
SM $t\bar{t}t$ modeling		
Cross-section		
Renormalization & factorization scale		
PDF		
Additional b -jets		
$t\bar{t}W$ modeling		
Renormalization & factorization scale		
Generator choice		
Additional b -jets		
$t\bar{t}Z$ modeling		
Cross-section		
Renormalization & factorization scale		
PDF		
Generator choice		
Additional b -jets		
$t\bar{t}H$ modeling		
Cross-section		
Renormalization & factorization scale		
PDF		
Generator choice		
Parton shower model		
Additional b -jets		
Other background modeling		
Cross-section		
Additional b -jets		

Table 7.3: Caption

Systematic uncertainty	Terms	Scale [%]
Reducible SM background		
$t\bar{t}/V/t+\text{jets}$	2	
Charge misidentification	1	
Fake & non-prompt background		
Low γ^*	1	
Material conversion	1	
HF e	1	
HF μ	1	
Light-flavor decays	1	100
Other fakes	1	30

Chapter 8. Results

8.1 Statistical analysis

This section provides an overview of the statistical methods needed to interpret the collected and simulated data to estimate unknown physics parameters and determine compatibility between data and the analysis hypothesis. For the BSM resonance search, the null hypothesis H_0 assumes only SM background contributions and none from any new resonance in the data.

8.1.1 Profile likelihood fit

Given a set of observed data points $\mathbf{x} = [x_1, x_2, \dots]$ and unknown parameters $\boldsymbol{\theta} = [\theta_1, \theta_2, \dots, \theta_n]$, the maximum likelihood method aims to find an estimate $\hat{\boldsymbol{\theta}}$ that maximizes the joint probability function $f(\mathbf{x}, \boldsymbol{\theta})$, or in other words the set of parameters that gives the highest probability of observing the collected data points for a particular model. The function to be maximized for this purpose is the log-likelihood (LLH) function $\ln \mathcal{L}(\mathbf{x}, \boldsymbol{\theta})$ where $\mathcal{L}(\mathbf{x}, \boldsymbol{\theta}) \equiv \prod_i f(x_i, \boldsymbol{\theta})$ is defined as the likelihood (LH) function. The LLH is maximized when $\partial/\partial\theta_i (\ln \mathcal{L}) = 0$ for each parameter θ_i .

For an usual binned physics analysis, the above variables for the LH function \mathcal{L} can be expressed as nuisance parameters (NP) $\boldsymbol{\theta}$ and number of events for a model $N_i(\mu)$ for the i^{th} bin, where μ is the targeted parameter of interest (POI). In this analysis, N_i is assumed to follow a Poisson distribution and depends on the following quantities: the signal strength μ defined as the ratio of observed to expected cross sections $\sigma_{\text{obs}}/\sigma_{\text{exp}}$; nuisance parameters $\boldsymbol{\theta}$ which represents the effects of systematic uncertainties, implemented in the LH function as Gaussian constraints; and normalization factors (NFs) $\boldsymbol{\lambda}$ that control the

1361 normalization of background components that do not have a well-known cross section. The
 1362 Poisson probability of observing exactly N_i events for an expected number of event n_i is

$$\mathcal{P}(N_i|n_i(\mu, \boldsymbol{\lambda})) = \frac{n_i^{N_i} e^{-n_i}}{N_i!}. \quad (8.1)$$

1363 The expected Poisson event number in a bin i can be parameterized as

$$n_i = \mu s_i(\boldsymbol{\theta}) + \sum_j \lambda_j b_{ij}(\boldsymbol{\theta}), \quad (8.2)$$

1364 where s_i is the number of signal events in bin i of every region, and b_{ij} is the number of
 1365 events for a certain background source index j in bin i . The LH function in this analysis
 1366 can be written as

$$\mathcal{L}(\mathbf{N}|\mu, \boldsymbol{\theta}, \boldsymbol{\lambda}) = \left(\prod_i \mathcal{P}(N_i|n_i) \right) \cdot \prod_k \mathcal{G}(\theta_k), \quad (8.3)$$

1367 where $\mathcal{G}(\theta_k)$ is the Gaussian constraint for a NP k . The signal significance μ and NFs $\boldsymbol{\lambda}$ are
 1368 left unconstrained and are fitted simultaneously in the profile LH fit. From Neyman-Person
 1369 lemma [citation](#), the optimal test statistic for hypothesis testing is a function dependent on
 1370 the profile LH ratio defined as

$$q_\mu \equiv -2 \ln \frac{\mathcal{L}(\mu, \hat{\boldsymbol{\theta}}_\mu, \hat{\boldsymbol{\lambda}}_\mu)}{\mathcal{L}(\hat{\mu}, \hat{\boldsymbol{\theta}}, \hat{\boldsymbol{\lambda}})}, \quad (8.4)$$

1371 where $\hat{\mu}$, $\hat{\boldsymbol{\theta}}$ and $\hat{\boldsymbol{\lambda}}$ are parameter values that optimally maximizes the LH function, and $\hat{\boldsymbol{\theta}}_\mu$,
 1372 $\hat{\boldsymbol{\lambda}}_\mu$ are NP and NF values respectively that maximize the LH function for a given μ .

8.1.2 Exclusion limits

8.2 Fit results

Fit setup

- Plain Asimov fit (**only mentioning briefly**): all regions included; simulated data used in the fit match exactly to MC prediction with nominal $\mu_{t\bar{t}Z'}$ set to 0 and allowed to free-float.

Purpose: to perform studies on optimizing fitted parameters and expected sensitivity; refining background estimation techniques; optimizing region definition and object definition

- Real SRs-blinded fit: similar to plain Asimov, but use observed data in CRs.

Purpose: study the behavior of background estimation using real observed data in CRs on Asimov data in SRs and assessing the influence of statistical effects on fitted parameters and expected sensitivity

- Real SRs-unblinded/ H_T fit: all regions included,

Limits

1388 **Chapter 9. Summary**

References

- [1] ATLAS Collaboration. *The ATLAS Experiment at the CERN Large Hadron Collider*. JINST 3 (2008), S08003 (cit. on p. 2).
- [2] C. Burgard and D. Galbraith. *Standard Model of Physics*. URL: <https://texample.net/model-physics/> (visited on 06/02/2025) (cit. on p. 4).
- [3] CMS Collaboration. *Search for $t\bar{t}H$ production in the $H \rightarrow b\bar{b}$ decay channel with leptonic $t\bar{t}$ decays in proton–proton collisions at $\sqrt{s} = 13$ TeV*. JHEP 03 (2019), p. 026. arXiv: 1804.03682 [hep-ex] (cit. on p. 7).
- [4] A. Pich. *The Standard Model of electroweak interactions. 2004 European School of High-Energy Physics*. Feb. 2005, pp. 1–48. arXiv: hep-ph/0502010 [hep-ex] (cit. on p. 13).
- [5] P. Higgs. *Broken symmetries and the masses of gauge bosons*. Phys. Rev. Lett. 13 (16 1964), pp. 508–509 (cit. on p. 13).
- [6] P. Higgs. *Broken symmetries, massless particles and gauge fields*. Physics Letters 12.2 (1964), pp. 132–133. ISSN: 0031-9163 (cit. on p. 13).
- [7] F. Englert and R. Brout. *Broken Symmetry and the Mass of Gauge Vector Mesons*. Phys. Rev. Lett. 13 (9 1964), pp. 321–323 (cit. on p. 13).

- [8] ATLAS Collaboration. *Observation of a new particle in the search for the Standard Model Higgs boson with the ATLAS detector at the LHC*. *Phys. Lett. B* 716 (2012), p. 1. arXiv: 1207.7214 [hep-ex] (cit. on p. 14).
- [9] CMS Collaboration. *Observation of a new boson at a mass of 125 GeV with the CMS experiment at the LHC*. *Phys. Lett. B* 716 (2012), p. 30. arXiv: 1207.7235 [hep-ex] (cit. on p. 14).
- [10] J. Ellis. *Higgs Physics. 2013 European School of High-Energy Physics*. 2015, pp. 117–168. arXiv: 1312.5672 [hep-ph] (cit. on pp. 15, 16).
- [11] P. Langacker. *The Physics of Heavy Z' Gauge Bosons*. *Rev. Mod. Phys.* 81 (2009), pp. 1199–1228. arXiv: 0801.1345 [hep-ph] (cit. on pp. 16, 17).
- [12] G. Ferretti and D. Karateev. *Fermionic UV completions of composite Higgs models*. *Journal of High Energy Physics* 2014.3 (Mar. 2014). ISSN: 1029-8479 (cit. on p. 17).
- [13] L. Vecchi. *A dangerous irrelevant UV-completion of the composite Higgs*. *JHEP* 02 (2017), p. 094. arXiv: 1506.00623 [hep-ph] (cit. on p. 17).
- [14] K. Agashe, A. Delgado, M. J. May, and R. Sundrum. *$RS1$, custodial isospin and precision tests*. *JHEP* 08 (2003), p. 050. arXiv: hep-ph/0308036 [hep-ph] (cit. on p. 17).
- [15] K. Agashe, R. Contino, and A. Pomarol. *The Minimal composite Higgs model*. *Nucl. Phys. B* 719 (2005), pp. 165–187. arXiv: hep-ph/0412089 [hep-ph] (cit. on p. 17).
- [16] N. Greiner, K. Kong, J.-C. Park, S. C. Park, and J.-C. Winter. *Model-independent production of a top-philic resonance at the LHC*. *Journal of High Energy Physics* 2015.4 (2015), p. 29. ISSN: 1029-8479 (cit. on pp. 17–19).

- [17] J. H. Kim, K. Kong, S. J. Lee, and G. Mohlabeng. *Probing TeV scale top-philic resonances with boosted top-tagging at the high luminosity LHC*. *Phys. Rev. D* 94 (3 2016), p. 035023 (cit. on p. 17).
- [18] ATLAS Collaboration. *Standard Model Summary Plots October 2023*. ATL-PHYS-PUB-2023-039. 2023. URL: <https://cds.cern.ch/record/2882448> (cit. on p. 23).
- [19] ATLAS Collaboration. *Electron reconstruction and identification in the ATLAS experiment using the 2015 and 2016 LHC proton–proton collision data at $\sqrt{s} = 13$ TeV*. *Eur. Phys. J. C* 79 (2019), p. 639. arXiv: 1902.04655 [[physics.ins-det](#)] (cit. on pp. 26, 39–41).
- [20] ATLAS Collaboration. *Performance of the ATLAS track reconstruction algorithms in dense environments in LHC Run 2*. *Eur. Phys. J. C* 77 (2017), p. 673. arXiv: 1704.07983 [[hep-ex](#)] (cit. on p. 31).
- [21] T. Cornelissen et al. *Concepts, design and implementation of the ATLAS New Tracking (NEWT)*. Tech. rep. Geneva: CERN, 2007. URL: <https://cds.cern.ch/record/1020106> (cit. on p. 31).
- [22] A. Salzburger and on behalf of the ATLAS Collaboration. *Optimisation of the ATLAS Track Reconstruction Software for Run-2*. *Journal of Physics: Conference Series* 664.7 (2015), p. 072042 (cit. on p. 31).
- [23] R. Frühwirth. *Application of Kalman filtering to track and vertex fitting*. *Nucl. Instrum. Methods Phys. Res. A* 262.2 (1987), pp. 444–450. ISSN: 0168-9002 (cit. on p. 31).
- [24] T. Cornelissen et al. *The global χ^2 track fitter in ATLAS*. *Journal of Physics: Conference Series* 119.3 (2008), p. 032013 (cit. on p. 31).

- [25] ATLAS Collaboration. *Improved electron reconstruction in ATLAS using the Gaussian Sum Filter-based model for bremsstrahlung*. ATLAS-CONF-2012-047. 2012. URL: <https://cds.cern.ch/record/1449796> (cit. on p. 31).
- [26] D. Wicke. *A new algorithm for solving tracking ambiguities*. Tech. rep. Oct. 1998. URL: <https://cds.cern.ch/record/2625731> (cit. on p. 32).
- [27] ATLAS Collaboration. *Reconstruction of primary vertices at the ATLAS experiment in Run 1 proton–proton collisions at the LHC*. *Eur. Phys. J. C* **77** (2017), p. 332. arXiv: 1611.10235 [[physics.ins-det](#)] (cit. on p. 32).
- [28] W. Waltenberger, R. Frühwirth, and P. Vanlaer. *Adaptive vertex fitting*. *Journal of Physics G: Nuclear and Particle Physics* **34.12** (2007), N343 (cit. on p. 32).
- [29] ATLAS Collaboration. *Secondary vertex finding for jet flavour identification with the ATLAS detector*. ATL-PHYS-PUB-2017-011. 2017. URL: <https://cds.cern.ch/record/2270366> (cit. on p. 32).
- [30] W. Lampl et al. *Calorimeter clustering algorithms: description and performance*. ATL-LARG-PUB-2008-002. 2008. URL: <https://cds.cern.ch/record/1099735>.
- [31] ATLAS Collaboration. *Topological cell clustering in the ATLAS calorimeters and its performance in LHC Run 1*. *Eur. Phys. J. C* **77** (2017), p. 490. arXiv: 1603.02934 [[hep-ex](#)] (cit. on pp. 33, 34).
- [32] ATLAS Collaboration. *Measurements of b -jet tagging efficiency with the ATLAS detector using $t\bar{t}$ events at $\sqrt{s} = 13$ TeV*. *JHEP* **08** (2018), p. 089. arXiv: 1805.01845 [[hep-ex](#)] (cit. on p. 36).

- [33] ATLAS Collaboration. *Graph Neural Network Jet Flavour Tagging with the ATLAS Detector*. ATL-PHYS-PUB-2022-027. 2022. URL: <https://cds.cern.ch/record/2811135> (cit. on p. 37).
- [34] A. Duperrin. *Flavour tagging with graph neural networks with the ATLAS detector*. Tech. rep. Presented at DIS2023, Michigan State University, USA. Geneva: CERN, 2023. arXiv: [2306.04415](https://arxiv.org/abs/2306.04415) [[hep-ex](#)]. URL: <https://cds.cern.ch/record/2860610> (cit. on p. 37).
- [35] S. Van Stroud et al. *FTAG Run-3 Algorithms Performance*. Tech. rep. Geneva: CERN, 2023. URL: <https://cds.cern.ch/record/2872884> (cit. on p. 37).
- [36] ATLAS Collaboration. *Electron and photon performance measurements with the ATLAS detector using the 2015–2017 LHC proton–proton collision data*. [JINST 14 \(2019\), P12006](#). arXiv: [1908.00005](https://arxiv.org/abs/1908.00005) [[hep-ex](#)] (cit. on pp. 39–41).
- [37] ATLAS Collaboration. *Electron Identification with a Convolutional Neural Network in the ATLAS Experiment*. ATL-PHYS-PUB-2023-001. 2023. URL: <https://cds.cern.ch/record/2850666> (cit. on p. 41).
- [38] ATLAS Collaboration. *Muon reconstruction and identification efficiency in ATLAS using the full Run 2 pp collision data set at $\sqrt{s} = 13$ TeV*. [Eur. Phys. J. C 81 \(2021\), p. 578](#). arXiv: [2012.00578](https://arxiv.org/abs/2012.00578) [[hep-ex](#)] (cit. on p. 43).
- [39] ATLAS Collaboration. *Muon reconstruction performance of the ATLAS detector in proton–proton collision data at $\sqrt{s} = 13$ TeV*. [Eur. Phys. J. C 76 \(2016\), p. 292](#). arXiv: [1603.05598](https://arxiv.org/abs/1603.05598) [[hep-ex](#)] (cit. on p. 43).

- [40] ATLAS Collaboration. *Performance of missing transverse momentum reconstruction with the ATLAS detector using proton–proton collisions at $\sqrt{s} = 13$ TeV*. *Eur. Phys. J. C* **78** (2018), p. 903. arXiv: 1802.08168 [[hep-ex](#)] (cit. on p. 44).
- [41] ATLAS Collaboration. *E_T^{miss} performance in the ATLAS detector using 2015–2016 LHC pp collisions*. ATLAS-CONF-2018-023. 2018. URL: <https://cds.cern.ch/record/2625233> (cit. on p. 45).
- [42] ATLAS Collaboration. *Observation of electroweak production of two jets in association with an isolated photon and missing transverse momentum, and search for a Higgs boson decaying into invisible particles at 13 TeV with the ATLAS detector*. *Eur. Phys. J. C* **82** (2022), p. 105. arXiv: 2109.00925 [[hep-ex](#)] (cit. on p. 45).
- [43] J. Alwall et al. *The automated computation of tree-level and next-to-leading order differential cross sections, and their matching to parton shower simulations*. *JHEP* **07** (2014), p. 079. arXiv: 1405.0301 [[hep-ph](#)] (cit. on pp. 48, 50, 51).
- [44] NNPDF Collaboration, R. D. Ball, et al. *Parton distributions for the LHC run II*. *JHEP* **04** (2015), p. 040. arXiv: 1410.8849 [[hep-ph](#)] (cit. on pp. 48, 50, 51).
- [45] T. Sjöstrand et al. *An introduction to PYTHIA 8.2*. *Comput. Phys. Commun.* **191** (2015), p. 159. arXiv: 1410.3012 [[hep-ph](#)] (cit. on pp. 48, 50, 51).
- [46] ATLAS Collaboration. *ATLAS Pythia 8 tunes to 7 TeV data*. ATL-PHYS-PUB-2014-021. 2014. URL: <https://cds.cern.ch/record/1966419> (cit. on pp. 50, 51).
- [47] S. Frixione, E. Laenen, P. Motylinski, and B. R. Webber. *Angular correlations of lepton pairs from vector boson and top quark decays in Monte Carlo simulations*. *JHEP* **04** (2007), p. 081. arXiv: [hep-ph/0702198](#) (cit. on p. 50).

- [48] P. Artoisenet, R. Frederix, O. Mattelaer, and R. Rietkerk. *Automatic spin-entangled decays of heavy resonances in Monte Carlo simulations*. [JHEP 03 \(2013\), p. 015](#). arXiv: [1212.3460 \[hep-ph\]](#) (cit. on p. 50).
- [49] D. J. Lange. *The EvtGen particle decay simulation package*. [Nucl. Instrum. Meth. A 462 \(2001\), p. 152](#) (cit. on p. 50).
- [50] R. Frederix, D. Pagani, and M. Zaro. *Large NLO corrections in $t\bar{t}W^\pm$ and $t\bar{t}t\bar{t}$ hadroproduction from supposedly subleading EW contributions*. [JHEP 02 \(2018\), p. 031](#). arXiv: [1711.02116 \[hep-ph\]](#) (cit. on p. 50).
- [51] E. Bothmann et al. *Event generation with Sherpa 2.2*. [SciPost Phys. 7.3 \(2019\), p. 034](#). arXiv: [1905.09127 \[hep-ph\]](#) (cit. on pp. 50, 51).
- [52] S. Schumann and F. Krauss. *A parton shower algorithm based on Catani–Seymour dipole factorisation*. [JHEP 03 \(2008\), p. 038](#). arXiv: [0709.1027 \[hep-ph\]](#) (cit. on p. 50).
- [53] S. Höche, F. Krauss, M. Schönherr, and F. Siegert. *A critical appraisal of NLO+PS matching methods*. [JHEP 09 \(2012\), p. 049](#). arXiv: [1111.1220 \[hep-ph\]](#) (cit. on p. 50).
- [54] S. Höche, F. Krauss, M. Schönherr, and F. Siegert. *QCD matrix elements + parton showers. The NLO case*. [JHEP 04 \(2013\), p. 027](#). arXiv: [1207.5030 \[hep-ph\]](#) (cit. on p. 50).
- [55] S. Catani, F. Krauss, B. R. Webber, and R. Kuhn. *QCD Matrix Elements + Parton Showers*. [JHEP 11 \(2001\), p. 063](#). arXiv: [hep-ph/0109231](#) (cit. on p. 50).
- [56] S. Höche, F. Krauss, S. Schumann, and F. Siegert. *QCD matrix elements and truncated showers*. [JHEP 05 \(2009\), p. 053](#). arXiv: [0903.1219 \[hep-ph\]](#) (cit. on p. 50).

- [57] F. Cascioli, P. Maierhöfer, and S. Pozzorini. *Scattering Amplitudes with Open Loops*. *Phys. Rev. Lett.* **108** (2012), p. 111601. arXiv: 1111.5206 [hep-ph] (cit. on p. 50).
- [58] A. Denner, S. Dittmaier, and L. Hofer. *COLLIER: A fortran-based complex one-loop library in extended regularizations*. *Comput. Phys. Commun.* **212** (2017), pp. 220–238. arXiv: 1604.06792 [hep-ph] (cit. on p. 50).
- [59] F. Buccioni et al. *OpenLoops 2*. *Eur. Phys. J. C* **79.10** (2019), p. 866. arXiv: 1907.13071 [hep-ph] (cit. on p. 50).
- [60] ATLAS Collaboration. *Analysis of $t\bar{t}H$ and $t\bar{t}W$ production in multilepton final states with the ATLAS detector*. ATLAS-CONF-2019-045. 2019. URL: <https://cds.cern.ch/record/2693930> (cit. on p. 62).
- [61] ATLAS Collaboration. *Measurement of the total and differential cross-sections of $t\bar{t}W$ production in pp collisions at $\sqrt{s} = 13$ TeV with the ATLAS detector*. *JHEP* **05** (2024), p. 131. arXiv: 2401.05299 [hep-ex] (cit. on p. 62).
- [62] ATLAS Collaboration. *Evidence for $t\bar{t}t\bar{t}$ production in the multilepton final state in proton–proton collisions at $\sqrt{s} = 13$ TeV with the ATLAS detector*. *Eur. Phys. J. C* **80** (2020), p. 1085. arXiv: 2007.14858 [hep-ex] (cit. on p. 62).
- [63] ATLAS Collaboration. *Observation of four-top-quark production in the multilepton final state with the ATLAS detector*. *Eur. Phys. J. C* **83** (2023), p. 496. arXiv: 2303.15061 [hep-ex] (cit. on p. 62).
- [64] ATLAS Collaboration. *Search for R -parity-violating supersymmetry in a final state containing leptons and many jets with the ATLAS experiment using $\sqrt{s} = 13$ TeV proton–proton collision data*. *Eur. Phys. J. C* **81** (2021), p. 1023. arXiv: 2106.09609 [hep-ex] (cit. on p. 62).

- 1559 [65] E. Gerwick, T. Plehn, S. Schumann, and P. Schichtel. *Scaling Patterns for QCD Jets*.
1560 [JHEP 10 \(2012\), p. 162](#). arXiv: [1208.3676 \[hep-ph\]](#) (cit. on pp. 62, 63).